

Geo 511  
Master's Thesis

# UNVEILING DEBRIS FLOWS

## Inferring debris-flow characteristics from vertical laser profile scanner data

Mylène Jacquemart  
09-722-620

supervised by:

Christoph Graf (WSL<sup>1</sup>)

Dr. Felix Morsdorf (RSL<sup>2</sup>)

Prof. Dr. Michael Schaepman (faculty representative, RSL<sup>2</sup>)

Submitted 30/1/2015

---

<sup>1</sup>*christoph.graf@wsl.ch*, Federal Research Institute WSL, Zürcherstrasse 111, 8903 Birmensdorf, Switzerland

<sup>2</sup>Remote Sensing Laboratories RSL, Department of Geography, University of Zurich, Winterthurerstrasse 190, 8057 Zurich, Switzerland

## **Acknowledgements**

This thesis would not have been completed without the help of many people around me. Special thanks go out to my two supervisors Christoph Graf and Felix Morsdorf, for their valuable input and guidance, and to Lorenz Meier, for providing his Matlab scripts as a starting point and his help and input throughout the last year.

Ethan Welty did a world-class job of correcting my thesis, contributing numerous valuable improvements. Also for their help with Matlab, corrections and other issues, I want to thank Nicolas Jacquemart, Beni Kuhn, Dominik Jäger, Annina Brügger, Alex Ruff, Jenny Steiner, Simon Etter, Matthias Kuhn, Beni Kellenberger, Alex Schläppi and Tamara Widmer.

I particularly want to thank my parents and family for their support throughout all my years in school, making it possible for me to get some of the best education there is.

Last but not least, I want to thank all contributors to programming and information technology forums. Without their valuable answers to (other people's) questions, this work might never have been completed.

## Abstract

The monitoring systems at two well-known debris-flow channels in the Swiss Alps – Dorfbach (municipality of Randa, canton of Valais) and Spreitgraben (municipality of Guttannen, canton of Berne) – were each fitted with a pair of downward facing laser profile scanners. Since 2011 (Dorfbach) and 2012 (Spreitgraben), the scanners have profiled passing debris flows at rates of 50 to 75 Hz, recording several million cross-flow profiles with point densities of roughly 20 points per meter. This study presents a preliminary analysis of this unique dataset and provides a code package for a semi-automatic extraction of the principal debris-flow characteristics (flow height, peak discharge, total discharge, and spatially distributed flow velocity).

Results from 13 debris-flow events (12 at Dorfbach, one at Spreitgraben), as well as data from an indoor experiment, demonstrate that a large-scale Particle Image Velocimetry (PIV) approach can be used to derive flow velocities, and that these in turn can be used to compute hydrographs for recorded events. Changes in channel bed geometry due to erosion and deposition during events are the largest source of uncertainty in estimates of total discharge. Furthermore, velocity outliers may have lead to overestimating peak discharge in several cases, calling for further improvements to the evaluation algorithms to reduce the influence of single velocity values. Nevertheless, the scanners have been found to offer distinct advantages over the long-standing use of radar gauges and geophones, where measurement quality depends strongly on the sensor position relative to the debris-flow path. This novel application of PIV to concatenated laser profiles made it possible to compute discharge values for every recorded event, while the data from the established system only provided estimates in two cases.

Finally, to describe the surface geometry of the debris flows, fourth order polynomials were fit to the recorded profiles. From this, it has been possible to estimate the amount of flow height that debris flows gain by building their distinct surge fronts. Two "curvature factors" are proposed to describe this convex surface geometry, and the results suggest that debris flows can gain up to 10 % of their width in height and that this process can account for 50 % of total flow height. Although this surface convexity has been observed and even modeled, it has never been measured in the field up until now.

These datasets have by no means been explored to their full extent. Hopefully the methodology and "toolbox" that are presented in this work will facilitate future studies with this kind of data, promoting further improvements to debris-flow monitoring, understanding, and modeling.



## Zusammenfassung

Der Dorfbach (Gemeinde Randa, Kt. VS) und der Spreitgraben (Gemeinde Guttannen, Kt. BE) sind für ihre Murgänge seit Jahren bekannt. Als Teil der jeweiligen Murgang-Beobachtungs- und -Überwachungssysteme wurden in den Jahren 2011 (Dorfbach) und 2012 (Spreitgraben) jeweils zwei 2D Laserscanner installiert. Diese haben seit ihrer Inbetriebnahme dank hohen Scanraten von 50 Hz bzw. 75 Hz Millionen von Profile des Bachbetts aufgenommen – während Murgangereignissen. Die vorliegende Studie zeigt erstmals auf, wie diese Daten genutzt werden können, um Abflussmengen von Murgängen zu bestimmen.

Von den untersuchten Ereignissen haben 12 am Dorfbach und eines am Spreitgraben stattgefunden. Die Methode *large-scale Particle Image Velocimetry (PIV)* wurde erstmals auf einen Datensatz aus Laser-Profilen angewendet. Die Untersuchung hat gezeigt, dass sich damit die Fließgeschwindigkeiten der Murgänge bestimmen lassen, und damit auch die Abflüsse berechnet werden können. Die Veränderungen, die während eines Murgangs durch Erosion und Ablagerung im Bachbett stattfinden können, stellen die grössten Unsicherheiten in der Abflussberechnung dar. Die Maximalabflüsse werden möglicherweise überschätzt, weil einzelnen Geschwindigkeits-Ausreissern noch zu viel Gewicht zugesprochen wird. Trotzdem bieten die Scanner gegenüber dem bewährten System aus Radaren und Geophonen klare Vorteile, insbesondere weil sie viel weniger stark vom Fließweg des Murgangs abhängig sind. So konnten alle erfassten Ereignisse der letzten vier Jahre ausgewertet werden, während dies mit den Daten vom herkömmlichen System nur in zwei Ereignissen möglich war.

Des Weiteren wurden die einzelnen Profile auf ihre Geometrie untersucht, indem sie mit Polynomen vierten Grades angenähert wurden. Aus den Minima und Maxima der Kurven lässt sich sodann abschätzen, um wie viel Murgänge durch das Ausbilden ihrer grobkörnigen Fronten an Fließhöhe gewinnen können. Zwei "Kurvaturfaktoren" werden vorgeschlagen, um diese Charakteristik zu beschreiben. Die Resultate deuten darauf hin, dass Murgänge bis zu 10 % ihrer Breite an Höhe gewinnen können, und dass bis zu 50 % der maximalen Höhe von diesem Prozess stammen kann. Diese Messungen stellen weltweit die ersten ihrer Art dar.

Die Möglichkeiten, die diese Datensätze bieten, wurden mit dieser Studie bei weitem nicht ausgeschöpft. Die entwickelte "Toolbox" kann aber dazu beitragen, dass zukünftige Studien mit solchen Datensätzen unser Prozessverständnis sowie die Murgangüberwachung und -modellierung verbessern können.



# Contents

<b>1</b>	<b>Introduction</b>	<b>1</b>
1.1	Framework of this thesis . . . . .	2
1.2	State of the art . . . . .	2
1.2.1	Debris-flow monitoring . . . . .	2
1.2.2	Terrestrial laser scanning . . . . .	3
1.2.3	Large-scale Particle Image Velocimetry . . . . .	4
1.3	Study objectives and research questions . . . . .	5
<b>2</b>	<b>Data &amp; methods</b>	<b>7</b>
2.1	Study sites . . . . .	7
2.2	Data acquisition . . . . .	9
2.3	Data processing . . . . .	11
2.3.1	Raw data processing . . . . .	11
2.3.2	Filtering . . . . .	14
2.3.3	Flow depth computation . . . . .	15
2.3.4	Flow velocity computation using LSPIV . . . . .	15
2.3.5	Hydrograph computation . . . . .	19
2.4	Sensitivity analysis . . . . .	20
2.5	Indoor experiment . . . . .	21
2.6	Surface curvature description . . . . .	21
2.7	Reflectance data . . . . .	23
<b>3</b>	<b>Results</b>	<b>25</b>
3.1	Sensitivity analysis . . . . .	25
3.2	Indoor experiment . . . . .	29
3.3	Event evaluation . . . . .	31
3.4	Surface curvature analysis . . . . .	34

<b>4</b>	<b>Discussion</b>	<b>39</b>
4.1	Sensitivity analysis . . . . .	39
4.2	Indoor experiment . . . . .	41
4.3	Raw data: errors, interpolation, and filtering . . . . .	42
4.4	Bed geometry and flow depth computation . . . . .	44
4.5	Displacement analysis using LSPIV . . . . .	46
4.6	Hydrograph generation . . . . .	49
4.7	Surface curvature . . . . .	51
4.8	Operational value . . . . .	52
<b>5</b>	<b>Conclusion</b>	<b>55</b>
<b>A</b>	<b>Technical summaries</b>	<b>65</b>
A.1	SICK LMS 511 laser scanner . . . . .	65
<b>B</b>	<b>Flow depths results</b>	<b>66</b>
<b>C</b>	<b>Flow velocity results</b>	<b>71</b>
<b>D</b>	<b>Experiment flow velocities</b>	<b>74</b>
<b>E</b>	<b>Technical documentation</b>	<b>75</b>
E.1	A: Raw data processing . . . . .	75
E.2	B: Debris flow analysis . . . . .	78



# List of Figures

2.1	Scanner platform and scan pattern . . . . .	12
2.2	Data processing flow diagram . . . . .	13
2.3	YXT coordinate system . . . . .	14
2.4	Window size dependencies . . . . .	17
2.5	LSPIV schematic . . . . .	17
2.6	Flow velocities (example) . . . . .	20
2.7	Experiment impressions . . . . .	22
2.8	Surface curvature schematic and debris-flow profile . . . . .	23
3.1	Influence of settings inconsistency . . . . .	30
3.2	Flow depth results from experiment . . . . .	31
3.3	Field flow depth results (example) . . . . .	32
3.4	Field flow velocity results . . . . .	33
3.5	Hydrograph results 1 . . . . .	35
3.6	Hydrograph results 2 . . . . .	36
3.7	Surface curvature results . . . . .	37
4.1	Shadowing effect . . . . .	45
4.2	Bed level changes . . . . .	46
4.3	Surge front differences . . . . .	48
B.1	Flow depth results B–D . . . . .	67
B.2	Flow depth results E–G . . . . .	68
B.3	Flow depth results H–L . . . . .	69
B.4	Flow depth results M . . . . .	70
C.1	Flow depth results A–F2 . . . . .	72
C.2	Flow depth results F3–M . . . . .	73
D.1	Flow velocities from indoor experiment . . . . .	74

E.1	Coordinate transformation . . . . .	76
-----	-------------------------------------	----

## List of Tables

2.1	Study sites summary . . . . .	8
2.2	Scanner settings . . . . .	11
3.1	Filtering influence . . . . .	27
3.2	Cross-correlation parameters . . . . .	28
3.3	Line averaging . . . . .	29
3.4	Experiment results . . . . .	30
A.1	Scanner technical summary . . . . .	65
E.1	Parameters for velocity computation . . . . .	79
E.2	OUTPUT-structure fields . . . . .	84

## List of Acronyms

IW	Interrogation Window
LSPIV	large-scale Particle Image Velocimetry
PIV	Particle Image Velocimetry
PTV	Particle Tracking Velocimetry
RPM	Revolutions Per Minute
SW	Search Window
SAR	Synthetic Aperture Radar
TLS	Terrestrial Laser Scanner

# 1 Introduction

Debris flows are gravity-induced mass movements common to mountainous regions around the globe, and their destructive power causes severe damage to infrastructure and livelihoods every year (e.g. Costa (1984)). Sharing characteristics of both floods and landslides, they are distinguished by high water content, very high velocities and a wide variation in transported materials, ranging from clay to large boulders (Hungri et al., 2001; Hungri, 2000). Oftentimes, multiple surges are recorded. Debris flows have the tendency to concentrate large grains at their surge head, which is followed by a watery tail (Pierson, 1986), resulting in a distinct longitudinal sorting and a convex cross section (Eisbacher & Clague, 1984; Colhoun, 1966).

As sediment availability in alpine regions is assumed to increase with rising temperatures (Gruber & Haeberli, 2009), changes to snowmelt and precipitation patterns have the potential to alter the frequency and magnitude of debris flows in the ever more densely populated alpine valleys (Huggel et al., 2012). Where infrastructure and livelihoods are threatened, mitigation measures are of utmost importance, but these can only be reliable through profound knowledge of the ongoing processes (Tobler et al., 2014; Graf et al., 2013). Insights from numerical modeling have become increasingly important for engineering structural mitigation measures and creating hazard maps (Rickenmann et al., 2006), and field observations of natural debris flows are essential to testing and improving these models (Hungri, 2000).

With regard to hazard mitigation, Hungri (2000) emphasizes the importance of peak discharge, peak velocities and flow depth as the main controls on a debris-flows' momentum, impact force, runout distance and ability to overrun channel walls and barriers. Modern debris-flow monitoring systems can provide measurements of these variables, and a wide variety of instruments has been used to achieve this (Arattano & Marchi, 2008; Itakura et al., 2005). The systems typically rely on geophones and ultrasonic- or radar gauges, but measurements from these sensors are sensitive to the positioning relative to the flow path and require clearly defined surge fronts to measure velocities. In addition, different authors have voiced the need to better understand and quantify the observed longitudinal sorting of grain sizes in debris flows (Iverson et al., 2010; Hungri, 2000).

This study presents a method relying on the image analysis technique Particle Image Velocimetry, free of the drawbacks described above, for measuring *peak discharge*, *flow depth*, *flow velocity* and *total discharge* of debris flows. Furthermore, an approach to describing the surface convexity related to the longitudinal sorting is proposed. A pair of high-frequency down-facing laser profile scanners was installed at each of two established debris-flow monitoring sites in the Swiss Alps, Dorfbach (canton of Valais) and Spreitgraben (canton of Bern), and the scanners provide a globally unique dataset featuring millions of cross-flow laser profiles recorded during thirteen debris-flow events. The detailed research questions are presented under point 1.3 on page 5.

## 1.1 Framework of this thesis

The scanners were installed at Dorfbach as part of the Swiss Federal Institute for Forest, Snow and Landscape Research (WSL) project *Hazard mapping in Mattertal, VS: data acquisition and numerical modeling of debris flows*. The project has been officially completed, but the data acquired by the laser scanners was not comprehensively analyzed until now. At Spreitgraben, the scanners were installed as part of the extensive warning system, but serve only research purposes.

## 1.2 State of the art

### 1.2.1 Debris-flow monitoring

Debris-flow monitoring and warning system are considered to be passive hazard mitigation measures, often deployed where debris-flows threaten infrastructure and livelihoods but where constructional methods are not possible. Such a system can provide advance and/or real-time warning or serve only for monitoring purposes (Arattano & Marchi, 2008). In Switzerland, debris-flow research and monitoring efforts experienced a significant surge following the catastrophic 1978 debris-flow and flood events (Hürlimann et al., 2003). The monitoring stations at Dorfbach were installed in the late 1990s (Graf & McArdell, 2005), while Spreitgraben rose more recently to prominence, producing several very large debris flows 2009–2011, after which an extensive monitoring and warning system was established (Tobler et al., 2014).

Aside from the laser scanners, both systems rely on established technologies to detect and quantify events, and thus compare well to debris-flow monitoring systems in use around the world. Flow velocities are typically calculated from the time taken by a surge

front to travel between different sensors mounted in a channel, but measurements are not always straightforward: Ultrasonic and radar gauges need to be well centered over the flow, which can be problematic in wide channels where flow path can change. Geophones measure ground vibrations and depend on the subsurface characteristics (Hürlimann et al., 2003). They also need to be placed close to the flow to provide clear readings, and changes in flow path can also make this difficult. Video cameras also constitute common components of debris-flow surveillance installations, but only on very few occasions have they been used to derive debris-flow characteristics and quantities (Genevois et al., 2001; Arattano & Marchi, 2000; Arattano & Grattoni, 2000), even though they have the potential to yield spatially distributed velocities, at least during daylight hours. The high-frequency laser scanners used in this study have the distinct advantage that they do not require daylight, and applying image analysis techniques reduces the need for a clear surge front to compute velocities. Furthermore, their large scan angle of  $190^\circ$  can easily handle changes of flow paths.

Velocity and flow stage measurements have been combined with measurements of basal normal and shear stresses, fluid pore pressure and erosion rates in debris-flow channels to gain insight into debris-flow dynamics (e.g. Iverson et al. (2010); Berger et al. (2010); McArdell et al. (2007)). The characteristic coarse-grained fronts and watery tails, resulting in the steep rise and gradual decline of many debris-flow hydrographs, have been widely observed and described, and understanding this transition is essential to providing accurate models. Field observations have long established that these rheological characteristics can vary greatly within single events, and no single rheology can satisfyingly describe a debris flow (Iverson, 2003). Video data and observations also show that the coarse-grained bouldery fronts can build convex surfaces. These convex cross sections have been marginally mentioned by different authors (Schürch et al., 2011; Eisbacher & Clague, 1984; Colhoun, 1966), but have never been investigated in detail or quantified. The dataset from the laser scanners provides a unique opportunity to investigate this phenomenon (henceforth *surface curvature*).

### 1.2.2 Terrestrial laser scanning

Laser scanning and ranging have evolved significantly over the last decades and have become indispensable to many geoscience efforts. Laser ranging applications date back to the 1960s, but were restricted to simple surveying tasks for decades - culminating in the development of total stations and eventually modern terrestrial laser scanners (TLS) capable of producing vast 3-D point clouds of their environment (Shan & Toth,

2009). Since the turn of the century, terrestrial laser scanning applications have been used in a wide variety of tasks in both natural as well as man-made environments. An all but comprehensive list includes, for example, mapping of 3-dimensional forest structures (Schneider et al., 2014; Danson et al., 2007), detecting surface displacements in rock or ice (Kenner et al., 2014; Abellán et al., 2009) or creating 3-D models of buildings and man-made structures (Früh & Zakhor, 2001). Applied to debris flows, TLS data has been used to track changes in channel geometry, erosion and deposition as well as changes on debris fans before and after events (e.g. Staley et al. (2011); McCoy et al. (2010)), but performing laser scans in real-time, during the passing of a debris flow, is still rare.

The laser scanners that provided the data for this work differ from classical terrestrial laser scanners in that they record 2-D profiles, not 3-D point clouds. This allows the scanners to reach very high scan rates of up to 100 Hz. These types of scanners are in wide use in aviation, automation, logistics, transportation and robotics (e.g. Yoneda et al. (2014); Stahn & Stopp (2007); Biber et al. (2004); Mendes et al. (2004); Ye & Borenstein (2002)), but are new to debris-flow science. A similar scanner may have been used to measure flow depth in a debris-flow channel in Sakurajima, Japan, but Osaka et al. (2013) do not specify precisely.

### 1.2.3 Large-scale Particle Image Velocimetry

The method used to derive the flow velocities from the laser profiles is large-scale Particle Imaging Velocimetry (LSPIV), which calculates displacement vectors from repeat temporal observations of visual features. Developed from Particle Tracking Velocimetry (PTV) and Particle Image Velocimetry (PIV) (Li et al., 2013; Lloyd et al., 1995; Stevens & Coates, 1994), LSPIV approaches have more recently been successfully applied to larger scale problems (Muste et al., 2008; Fujita et al., 1998). The terms LSPIV and PIV are used interchangeably in literature, and no clear distinction will be made here either. All of the above are based on 2-D cross-correlation analysis, a common image analysis technique (Pan et al., 2009; Gonzalez & Woods, 2008) which has been applied to a variety of problems including tracking glacier, sea ice or cloud motion from optical as well as radar data (eg. Schubert et al. (2013); Im et al. (2008); Scambos et al. (1992); Leese et al. (1971)).

Being non-intrusive, LSPIV offers distinct advantages over other gauging techniques, and has proven suitable for measuring flow velocities during periods of high flow (Le Coz et al., 2010). In some cases, artificial seeding is used to generate well traceable particles, but studies tracking natural features such as the surface patterns of turbulent water or

floating vegetal debris have proven equally successful (Dobson et al., 2014; Zhang et al., 2013). In the laser version of LSPIV, the vertical (height) component is used as an equivalent of light intensity in photographic data. A number of teams have used repeat TLS point clouds to investigate the displacement fields of landslides and rock glaciers in this manner (e.g. (Travelletti et al., 2014; Kenner et al., 2014; Aryal et al., 2012)).

The present study differs from traditional LSPIV setup in several ways. Rather than working with repeat visible or near infrared photographs or TLS data, the two laser profile scanners were mounted a small distance apart to produce repeat distance profiles of the debris-flow channel. The details of the setup their implications to the processing required are described in chapter 2 on page 7.

### 1.3 Study objectives and research questions

The aim of this study was to assess the suitability of the SICK LSM511 laser profile scanners for debris-flow monitoring tasks. The data was collected during the debris-flow seasons of 2011–2014 and an indoor experiment was conducted in late 2014. This thesis focuses on describing and evaluating a code package that was developed in order to compute the principal debris-flow variables from the laser profiles. The study evaluates the potential of these types of datasets for research as well as their utility in operational debris-flow monitoring and warning systems. In order to achieve the aforementioned objectives, the following research questions were formulated:

1. Can debris-flow *height*, *velocity* and *total* and *peak discharge* be derived from the laser scanner data in an automated or semi-automated way?
  - 1.1. What are the the main sources of uncertainty, and how do they relate to the steps of raw data processing, bed geometry and flow depth computation, and displacement analysis and hydrograph generation?
  - 1.2. How do the main processing parameters *number of averaged files*, *correlation window size* and *lateral resolution* influence the processing results?
  - 1.3. What methodological insights can be gained from performing a controlled indoor experiment?
2. Can the laser scanner data be used to describe the surface curvature of a debris flow?
3. If so, can the surface curvature be quantified and does it relate to the physical characteristics?

The methodology applied is explained in detail in chapter 2 on page 7, followed by the results in chapter 3 (pp. 25) and an in-depth discussion of the findings (chapter 4, pp. 39). Chapter 5 on page 55 highlights the most important conclusions and offers a short outlook for further work.



## 2 Data & methods

### 2.1 Study sites

Both study sites are located in the Swiss Alps, in the municipalities of Randa (canton of Valais) and Guttannen (canton of Berne), where the scanners are components of extensive debris-flow warning and monitoring systems. Detailed descriptions of these installations can be found, for example, in Jacquemart et al. (2015), Tobler et al. (2014), and Graf et al. (2013). The setup at Dorfbach differs slightly from how it was described in Graf et al. (2013) as the upper station was moved several 100 m downriver and the lower station was dismantled in late summer 2013. Table 2.1 on page 8 provides an overview of the two locations, their key characteristics, and their instrumentation.

Both catchments have vivid debris-flow histories. Their debris cones are testament of debris-flow activity throughout the last centuries (Kober et al., 2012). The Spreitgraben was reactivated after a rock-fall event from the north east face of the Ritzlihorn in 2009, and produced several very large and extremely erosive precipitation-triggered debris flows in the two years following the rock fall event (Tobler et al., 2014). The Dorfbach is prone to smaller events, mostly triggered by snow melt during early summer months, as the Grabengufer rock glacier in the upper part of the catchment produces vast amounts of debris (Barboux et al. (2013); Delaloye et al. (2013)). While Spreitgraben is deeply incised into its debris fan, the channel bed at Dorfbach is about 20 m wide on average, allowing the flow path to change frequently.

Unfortunately, the scanners were not in place during any of the large events that took place at Spreitgraben, but one event was captured there in 2014. Seven days with debris-flow events were recorded at Dorfbach, sometimes featuring multiple events on a single day. Table 2.1 also lists the dates of all the observed debris flows. Capital letters in Table 2.1 denote the different events recorded throughout the last four years. Validation data for these events is very limited. Flow height information is available for most events from a radar gauge, but as these are 3 m footprint averages, they are difficult to compare against the narrow, spatially distributed laser measurements. The radar measures flow height in the channel based on the return time of emitted radar pulses. However, the

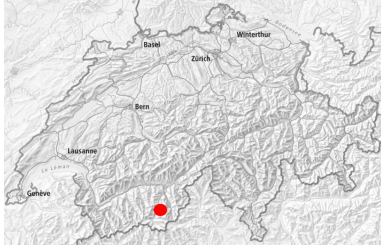
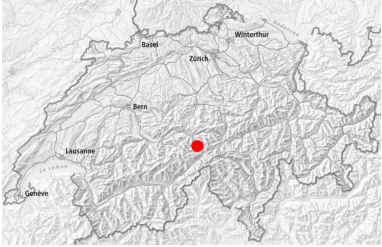


	Randa, VS	Guttannen, BE
Torrent	Dorfbach	Spreitgraben (Spreitlau)
		
		
Altitude	1396 ma.s.l. – 4547 ma.s.l.	943 ma.s.l. – 3263.1 ma.s.l.
Catchment size	5.7 km <sup>2</sup> (Graf et al., 2013)	4.7 km <sup>2</sup> (Tobler et al., 2014)
Aspect	WNW	NE
Geology	crystalline gneiss (Graf & McArdeU, 2005)	highly foliated gneisses of the Aare Massiv (Tobler et al., 2014)
Main debris source	Grabengufer rock glacier	Rock fall deposits from the Rit-zlihorn NE face
System purpose	Monitoring	Advance- and real time warn-ing, monitoring
Instrumentation as of 2014 (count)	Laser profile scanners (2), camera (1), radar gauge (1), weather station (1), geophones (4)	Laser profile scanners (2), cameras (4), radar gauge (2), weather station (1), geophones (2), trigger lines (6), FMCW radar (1), traffic lights (4)
Power supply	Solar panels	230V AC
Recorded events (denotation)	04.6.2011 (A, B) 03.6.2012 (C, D) 02.7.2012 (E, F) 18.6.2013 (G) 06.6.2014 (H) 11.6.2014 (J) 29.7.2014 (K,L)	30.8.2014 (M)

Table 2.1: Study site and monitoring system characteristics. The recorded events are assigned capital letters to simplify event referencing in the subsequent analysis. Maps from map.geo.admin.ch, photos by Christoph Graf (Dorfbach) and Geopraevent (Spreitgraben).

debris flows did not always pass directly underneath the radar gauge. Flow velocity data is only available for events A and B (4. June 2011), and consists of front velocities deduced from the geophone measurements. These readings of ground vibrations can be used to detect the passing of a debris flow, but the velocities are average front velocities over several hundred meters and upslope of the scanner position. For all other events, geophone data quality was not adequate to compute the flow velocity. Events A and B are therefore the only events for which validation data is available, and peak discharge, total discharge, maximum flow depth and (geophone-derived) front velocity are listed below:

**Event A:**  $18 \text{ m}^3\text{s}^{-1}$ ;  $1300 \text{ m}^3$ ;  $0.9 \text{ m}$ ;  $4.1 \text{ ms}^{-1}$

**Event B:**  $11 \text{ m}^3\text{s}^{-1}$ ;  $1100 \text{ m}^3$ ;  $0.5 \text{ m}$ ;  $2.4 \text{ ms}^{-1}$

## 2.2 Data acquisition

SICK model LMS 511 laser scanners were used in this study (see Appendix A for detailed technical specifications). A pair was installed at each of the two study sites, recording cross-flow profiles of debris flows at rates of 50-75 Hz. The scanners have a maximum scan angle of  $190^\circ$ , but it is usually not necessary to make use of the entire scan width in order to cover the width of a debris-flow channel (see Table 2.2 for details). Figure 2.1 on page 12 shows how the scanners are mounted below a platform suspended above the debris-flow channel with steel cables, and a schematic illustrates the 2-D scan acquisition. A close-up of the scanners can also be found in Figure 2.7 on page 22. The lasers are operated at a near-infrared wavelength of 905 nm, at which the mean reflectance of the sediment-water mixture is around 45% ( $\sigma = 8\%$ ). The scanners have the capacity of recording up to five returns, but only the last return is recorded in this setup.

At the Dorfbach site, the scanners are triggered by geophones; the data is stored locally and needs to be retrieved at regular intervals. At the Spreitgraben site, data is continuously written to a circular buffer and must to be downloaded after events, before the local memory is overwritten by new data. At both sites, the platform on which the scanners are mounted is also fitted with a radar gauge and a webcams faces the channel below the platform.

The scanner settings differ at the two locations and for individual years (see Table 2.2). The distance between the scanners on the platform is 79 cm, and this was changed in 2012 when the scanners were tilted slightly away from each other, enlarging the distance between them at the channel bed. The distance between the scanners needs to be known

for the velocity computation.

At Dorfbach, the scan rate was reduced from 75 to 50 Hz in 2012, which simultaneously increased the angular resolution from  $0.5^\circ$  to  $0.3333^\circ$ . The SICK LMS 511 deflects the laser pulses using a rotating mirror, and distances are measured within a polar coordinate system using time-of-flight measurements of the emitted pulses. Following Vosselman & Maas (2010) and the SICK product documentation (SICK, 2010), the laser footprint diameter  $D_s$  at a distance  $h$  from the scanner is defined as:

$$D_s = d_{\text{exit}} + 2h \tan \frac{\gamma}{2} \quad (2.1)$$

where  $d_{\text{exit}}=13$  mm is the ray diameter at the point where the laser beam leaves the scanner, and  $\gamma$  is the beam divergence of 11 mrad (Dorfbach) or 3.6 mrad (Spreitgraben). The distance between the scanners and the channel bed at Dorfbach has remained more or less constant at around 10 m, corresponding to a beam footprint of roughly 12 cm. At Spreitgraben, the distance  $h$  is approximately 20 m and the laser footprint diameter amounts to about 10 cm. The distance to the channel bed also defines the spacing between the measurement points, and a distance of 10 m results in a point spacing  $d_p$  of 9 cm and 6 cm for  $0.5^\circ$  and  $0.3333^\circ$ , respectively. For an object to be reliably detected, it must be entirely struck by at least the full width of one pulse, thus the minimum object size (at 10m distance and  $0.5^\circ$  angular resolution) is

$$D_{\text{obj}} = D_s + d_p \approx 9 \text{ cm} + 12 \text{ cm} = 21 \text{ cm} \quad (2.2)$$

for the geometry of the setup at Dorfbach, and roughly 30 cm at Spreitgraben.

The object size depends strongly on the distance, and will thus vary slightly across the bed. Depending on their surface and reflectance characteristics, smaller objects can certainly also be detected, but it is assumed that objects smaller than  $D_{\text{obj}}$  are not useful to the flow velocity computation because they will not stand out or persist as single features. Two relationships can be used to describe how objects are recorded by the spatiotemporal sampling of the scanners. In the cross-flow direction, surface roughness is smoothed somewhat during scanning if  $d_p < D_s$ . In the time dimension, the flow velocity and object size define how an object is mapped. The number of scan lines  $N$  striking an object is

$$N = \frac{\vec{v} \cdot \vec{s}}{L \cdot c},$$

where  $L$  is the object length,  $\vec{v}$  is the object velocity,  $\vec{s}$  is the sampling rate. The coefficient

c is 1 if the full temporal resolution of the files is used. If several lines are averaged in order to reduce the amount of data, the number of lines available for mapping an object is reduced accordingly.

Location	Year	Angular resolution	Scan angle setting	Scan rate	Distance between scanners at the channel bed
Dorfbach	2011	0.5°	-5 – 185°	75 Hz	79 cm
Dorfbach	2012	0.3333°	-5 – 185°	50 Hz	79 cm
Dorfbach	2013	0.3333°	-5 – 185°	50 Hz	≈129 cm*
Dorfbach	2014	0.3333°	-5 – 185°	50 Hz	≈129 cm*
Spreitgraben	2014	0.5°	10 – 170°	75 Hz	≈180 cm**

Table 2.2: Scanner settings at Dorfbach and Spreitgraben for 2011 – 2014. \*/\*\* scanners are slightly tilted, enlarging the actual distance between their scan lines. Distances resulting for 10 m (\*) and 20 m (\*\*).

## 2.3 Data processing

All data processing and analysis was performed in Matlab<sup>®</sup>, and the complete technical documentation can be found in the appendix (sections E). The code was not printed, but can be found on the CD handed in as part of this thesis or requested from the author. The raw data functions *ReadLMSFiles* and *ReadOneLMSFile* as well as the basic structure of the velocity computation were provided by Dr. Lorenz Meier (Geoprävent AG). The code that makes up the code package that is provided for the analysis is divided into three parts: Raw data processing, debris flow analysis and analysis of the surface curvature. The user is asked to specify parameter values as needed, while the computed results are saved for all important steps. After the initial development of the code, a sensitivity analysis was carried out in order to find suitable parameter sets for the final event evaluation, and an experiment was set up to validate the code. In the following, the data processing is described in more detail and illustrated in figure 2.2 on page 13.

### 2.3.1 Raw data processing

Scanner output consists of one file containing the time stamps and raw distance and reflectance values from both scanners, as well as scanner serial number, scanner status messages and other scanner metadata fields. The *ReadLMSFile* function converts the raw data values from hexadecimal to decimal, and extracts the scan line metadata so that the scan lines can be separated based on their scanner serial number.

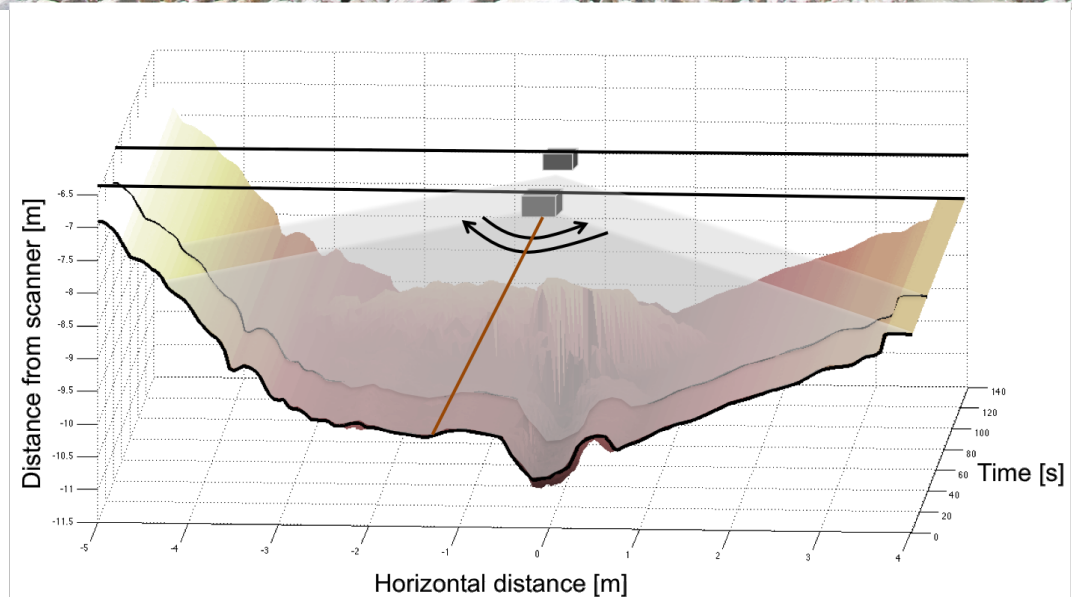
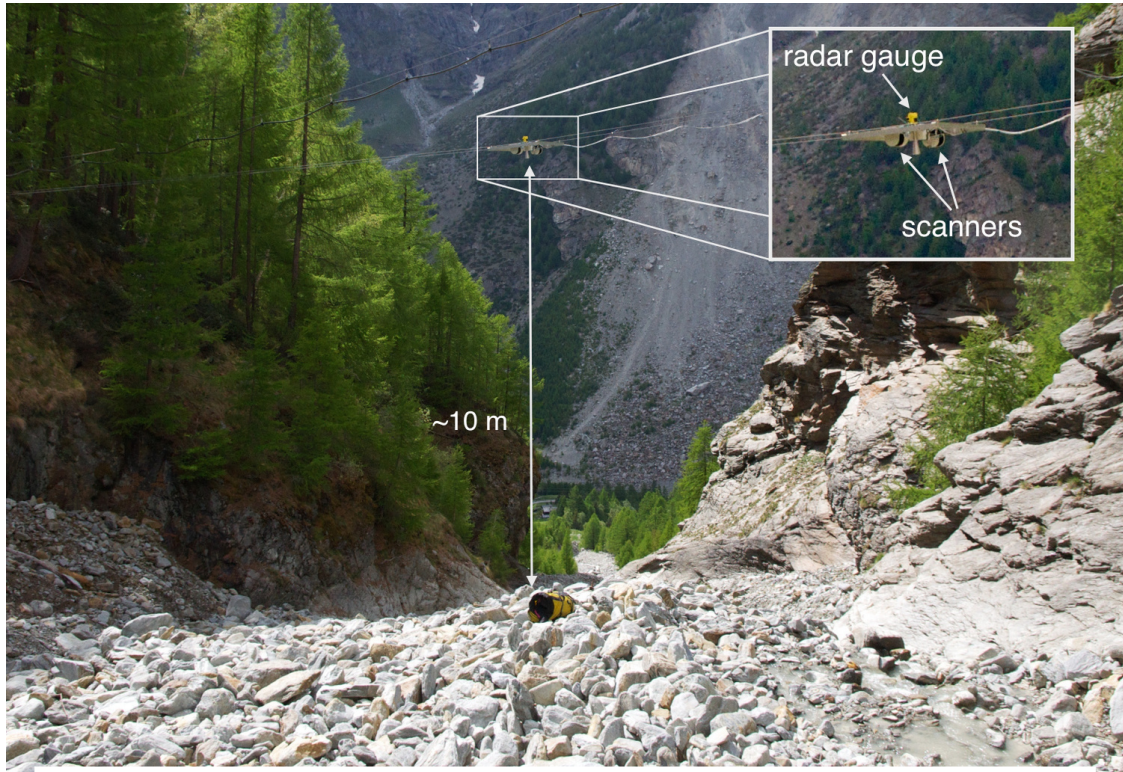


Figure 2.1: Scanner platform suspended above the Dorfbach debris-flow channel in Randa, Valais, Switzerland. The conical device visible between the scanners is the radar gauge. The schematic below illustrates the cross-flow scanning pattern.

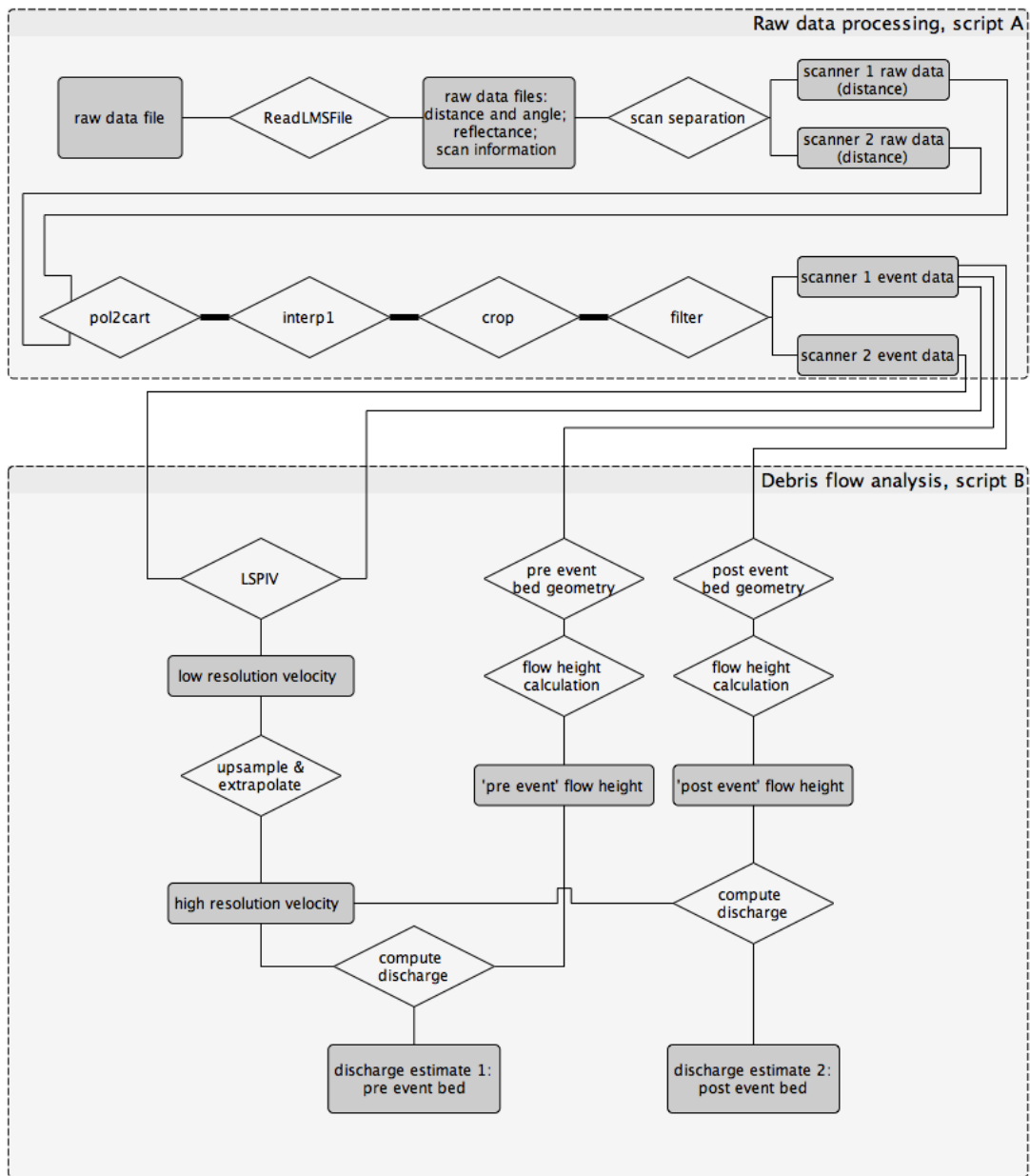


Figure 2.2: Data processing chain for the distance matrices used for the hydrograph computation. The processing of reflectivity values has been excluded for simplicity. Gray squares represent data matrices and diamonds represent processing steps. Bold lines are drawn where the processing steps are carried out separately for each of the two scanner datasets.

The raw distances in polar coordinates are first transformed into unevenly spaced cartesian coordinates, then interpolated onto a regular grid with a 5 cm spacing along the (cross-flow) x-axis. The event sequence of interest is isolated from the data, usually also narrowing the considered range along the x-axis for further computation (steps `pol2cart`, `interp1`, and `crop` in Figure 2.2). As a result, every observation can be described with a set of coordinates  $(y,x,t)$ , as depicted in figure 2.3. So while the scanners only record single-line profiles at a time, once all profile lines are concatenated along the time-axis, 2.5-D image-like matrices are generated, where x is the cross-flow distance in meters, t is the time in seconds and the matrix contains values of distance from the scanner in mm (y). Values falling below a certain user defined threshold (e.g. 4 m distance from the scanner) are substituted with NaN (Matlab's "Not-a-Number" value) because they are anomalously close to the scanner and assumed to be erroneous.

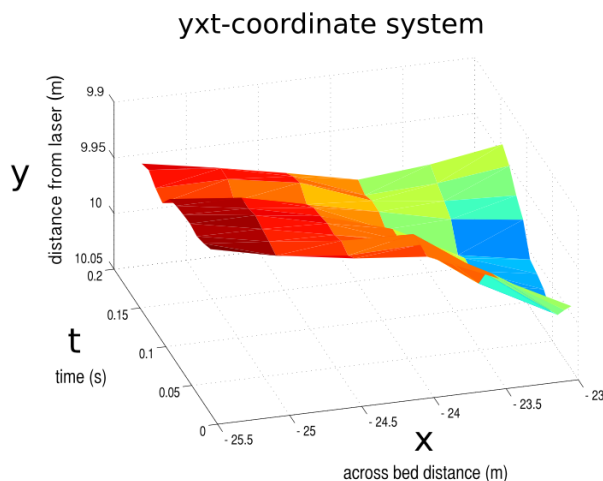


Figure 2.3: Individual xy-profiles are concatenated and plotted in time, resulting in a yxt coordinate system.

### 2.3.2 Filtering

Erroneous values in the raw data are assumed to be most often caused by splashing over the debris flow, but may also be attributable to rain or the dripping of water from the mounting platform.

To help smooth out noise, a 3x3 cells moving window median filter was applied to the data (Gonzalez & Woods, 2008). In order not to remove valuable surface roughness information however, the residuals between the original and the smoothed data were plotted, and only data points exceeding three standard deviations of the residual range



were removed. All the remaining points were returned to the filtered signal unchanged. In order to reduce the amount of data in processing, and to investigate the influence of temporal resolution, blocks of 3 (2), 5, 15 (10), 25, 75 (50) lines in time were averaged from the original files of 75 Hz (50 Hz) resolution data. The full resolution file (with no temporal averaging) was also retained, and the averaging was always performed after the noise filtering. The event evaluations performed for this study were all conducted using the full temporal resolution files.

### 2.3.3 Flow depth computation

In order to be able to compute hydrographs from the laser data, and thus derive the debris-flow characteristics *total* and *peak discharge*, a measure of flow depth is needed, which itself requires making assumptions about the geometry of the channel bed. A pre- and post-event bed geometry is computed by averaging ten seconds-worth of profiles before and after each event.

Once the bed geometry profile (*bedgeom*) is computed, the flow height for every point ( $x,y$ ) along  $t$  can be calculated as:

$$\text{FlowHeight}_{xt} = \begin{cases} 0, & \text{if } y_{xt} \leq \text{bedgeom}_x \\ y_{xt} - \text{bedgeom}_x, & \text{if } y_{xt} > \text{bedgeom}_x \end{cases} \quad (2.3)$$

The bed geometry is assumed to remain static during the entire duration of an event. This is not a realistic assumption, as debris flows are known to strongly erode their beds or fill them with debris, and both processes are possible during a single event (Berger et al., 2010). In order to assess the influence of assumed bed geometries, and to provide a possible range of uncertainty for the discharge estimation, results for every event were computed both with the the pre-event and post-event bed geometry. Data from either of the two scanners can be used to compute the flow depth, and differences should be small except when bed geometry changes significantly between the scanners. This was the case in 2011, when a large overdeepening formed below the second scanner. In the present study, the upslope scanner (scanner 1) was always used to compute the flow depth.

### 2.3.4 Flow velocity computation using LSPIV

Despite the differences between concatenated laser profiles and time lapse image data, LSPIV nevertheless offers a suitable methodological framework for the computation of flow velocities from repeat laser scanning results. The main difference is that the "images" used in the present study are recorded at two different locations simultaneously, rather

than at different times in one location. In the common LSPIV approach, velocity is computed as  $\vec{v} = l/\Delta t$ , where  $l$  is the spatial displacement measured by cross-correlation and  $\Delta t$  is the known temporal offset between the two images. In the present application, velocity is computed as  $\vec{v} = l_d/\Delta t$  where  $l_d$  is the known spatial distance between the two scanners and  $\Delta t$  is the temporal displacement as measured by cross-correlation. Since the measured displacement describes a temporal rather than a spatial offset, the image orthorectification process at the beginning of image-based LSPIV can be omitted. From this point forward, the displacement computation is essentially identical to the standard LSPIV as described in Dobson et al. (2014) or Le Coz et al. (2010). The data matrix from scanner 1 is divided into small subsets, or interrogation windows (IW) and an appropriate part of the data matrix from scanner 2 is searched for the closest match (search window; SW). The size of these windows has received significant attention in scientific literature. For classical PIV approaches, Raffel et al. (2007) state that the size of the SW must be at least three times larger than the maximum expected displacement within the IW, and Hu et al. (1998) emphasize that the IW must be smaller than the SW and at least twice the size of the maximum displacement so as not to violate the Nyquist theorem. Furthermore, Meunier & Leweke (2003) argue that the size of the IW must be large enough to contain a sufficient number of pixels with unique values to estimate a cross correlation function, preferably showing more than 10–20 particles. In the laser datasets, the temporal window width ("duration",  $l_t$ ) of these windows is defined by the expected flow velocities: For lower velocities, the data from the downflow scanner needs to be searched over a longer period of time, while for high velocities the lag (or "waiting time") to the start of the search window relative to that of the interrogation window needs to be kept short. The relationship between the temporal window width, the waiting time between the first and second scanner, and the expected flow velocities is described in Figure 2.4.

The maximum and minimum expected velocities as well as the lateral resolution need to be defined by the user. It is assumed that the lateral resolution can be defined based on the expected particle size. To allow for particles to move about freely, the SW is defined to be three times wider than the IW. As is commonly done, the cross-correlation coefficient is used as similarity index to find the displacement between the IW and the SW (Dobson et al., 2014; Le Coz et al., 2010; Muste et al., 2008). Figure 2.5 on page 17 illustrates the concept described above.

Based on the results of the sensitivity analysis (page 28), maximum expected velocity was set to  $20 \text{ ms}^{-1}$  ( $10 \text{ ms}^{-1}$  for the event at Spreitgraben), minimum expected velocity to  $0.1 \text{ ms}^{-1}$ , defining the temporal width of the correlation window. The spatial window

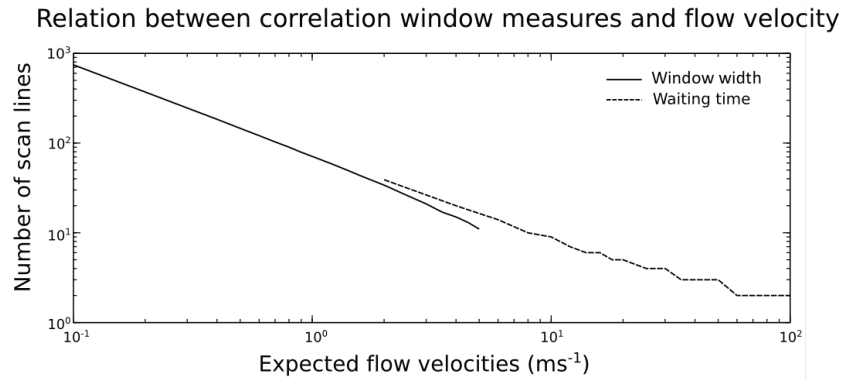


Figure 2.4: Exponential relationship between the temporal width of the IW and SW and the expected flow velocities. Low flow velocities require an increase in the time searched for a correlation. The maximum expected flow velocity determines the waiting time between the IW and SW. The stepped shape of the waiting time (dashed line) is a result of rounding to integer numbers of scan lines.

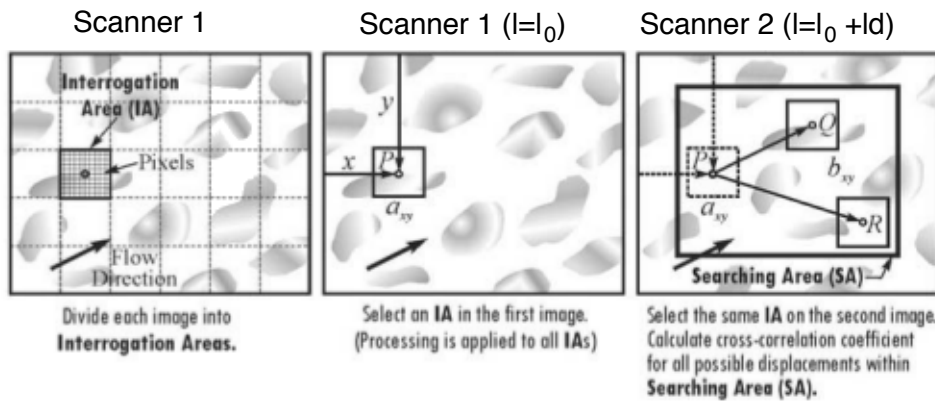


Figure 2.5: Illustration of LSPIV processing adapted from Muste et al. (2008). The term "area" was adapted to "window" in the present study because the image subsets have both spatial and temporal components.

width (*lateral resolution*) was set to 100 cm. An in depth discussion of these values is offered in chapters 3 and 4.

The cross-correlation analysis is conducted on a high pass filtered surface of the original data (Kenner et al., 2014), where the filtering is performed at the level of the IW and SW by calculating the difference for every point  $x, t$  to a second order polynomial fit to each data line along  $x$ . This removes the height offsets between the two scanners that may arise from differences in channel slope or platform inclination, leaving only the high frequency surface structure. The 2-D cross-correlation of an M-by-N matrix X and a P-by-Q matrix H is a matrix C of size M+P-1 by N+Q-1 given by (Mathworks, 2012):

$$C(k, l) = \sum_{m=0}^{M-1} \sum_{n=0}^{N-1} X(m, n) \bar{H}(m-k, n-l), \quad (2.4)$$

$$-(P-1) \leq k \leq M-1,$$

$$-(Q-1) \leq l \leq N-1$$

At every time step  $t_t/4$ , C is computed for the corresponding IW and SW. The output matrix C(k,l) has negative and positive row and column indices, and the location of the maximum in C describes the displacement a particle has experienced. This displacement represents the time taken by a particle to reach the downslope scanner, which is subsequently used to compute the flow velocity. An example of a flow velocity matrix is given in Figure 2.6 (left).

Since outside the travel path of the debris flow values in C should be very low because the scanner views remain different throughout, a normalized cross-correlation matrix is also computed for the whole image. This is done by retaining the maximum C for every window and normalizing these with the maximum C found across the all windows. Windows with normalized C smaller than 0.1 are then excluded. Furthermore, since debris is (reasonably) assumed to move only downslope, only the lower half of the cross-correlation matrix is searched for peak correlation values, thus excluding peaks that correspond to particles arriving at the downriver scanner before arriving at the upriver scanner.

Finally, to reduce the number of "false detections" (e.g. from splashes occurring in both the IW and the SW producing a high correlation coefficient), a quality criterion was introduced: This specifies that the peaks in the correlation coefficient matrix need to be wide enough to be assumed to come from a "real" particle, i.e. a rock transported on the surface of the debris flow. A maximum in C is considered valid if 18 out of 25 cells in the 5x5 cell neighborhood of the peak exhibit a value of 0.7 of the maximum itself

(a five cell wide neighborhood was chosen because it makes the width of the correlation peak just slightly more than the minimum detectable object size of 21 cm). If this criteria is not met, then the corresponding velocity cell is excluded from the further processing.

### 2.3.5 Hydrograph computation

The number of cells in the resulting velocity matrix depends on the number of steps computed along the time axis and the total width of the profiles divided by the lateral resolution. This matrix is first upsampled to the resolution of the flow depth matrix using nearest neighbor resampling.

Secondly, since in most cases the cross-correlation analysis will not provide velocity estimates for the entire debris flow, it becomes necessary to extrapolate (or interpolate) the velocities to areas where no estimate exists. The extrapolated velocity for a grid cell  $(x,t)$  is computed by multiplying the median measured flow velocity along the corresponding line  $t$  with the quotient of the flow height for that particular cell (i.e. the flow height at  $x,t$  divided by maximum flow height along  $t$ ). Any line  $t$  must thus have at least one velocity estimate for the extrapolation to be possible. Figure 2.6 on page 20 shows an example of the original low resolution velocity matrix, and the upsampled and extrapolated velocity matrix.

Computing the hydrograph is thence a straightforward sum along every line  $t$  and total discharge is simply the cumulative sum over the entire duration of the debris flow. This is described in equations 2.5 and 2.6, in which  $Q_t$  is the discharge across every line,  $X$  is the total number of cells in the cross-flow direction, flow height is in meters,  $L_c$  is the grid cell size [m],  $\vec{v}_{x,t}$  is the corresponding flow velocity,  $Q_{tot}$  is the total discharge,  $T$  is the total duration of the event in seconds and  $s$  is the sampling rate. For the final "best" estimate, gaps originating from lines along  $t$  with no velocity estimates are filled by computing discharge values from the event-wide mean velocity. Such gaps are clearly visible in Figure 2.6 at  $t=50$  s and  $t=125$  s.

$$Q_t = \sum_{x=1}^X \text{FlowHeight}_{x,t} \cdot L_c \cdot \vec{v}_{x,t} \quad (2.5)$$

$$Q_{tot} = \sum_{t=1}^T Q_t \cdot \frac{1}{s} \quad (2.6)$$

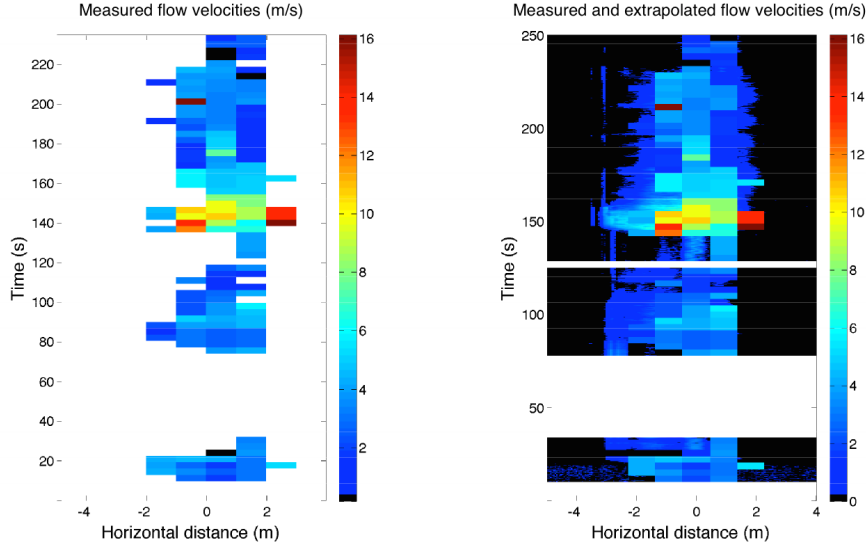


Figure 2.6: Left: Low resolution flow velocity matrix. The number of cells depends on the temporal width of the correlation window and the choice of lateral resolution. Right: High resolution flow velocity matrix after velocity extrapolation. Where no velocity estimate along  $x$  is available, no extrapolation is conducted.

## 2.4 Sensitivity analysis

A sensitivity analysis was performed to test the influence of the filtering, the quality criterion, the size of the SW relative to that of the IW, the number of averaged lines in  $t$ , the choice of maximum and minimum flow velocities, as well as the lateral resolution. In a first step, two datasets (A and G) were used to compare the effect of filtering, the quality criterion, the size of the SW and the number of averaged lines. To seek out the best performing parameter values for minimum and maximum expected velocities as well as lateral resolution, two additional datasets were included in the second step (K and M).

Aside from debris-flow characteristics (e.g. maximum flow depth, total discharge and peak discharge), the number of cells with cross-correlation velocities can also be used to indicate how well the chosen parameter values perform. It must be noted however, that this normalized *correlation count*  $C_{\text{count}}$  can only be drawn upon to compare results for the same event because it depends on the ratio between the "active" and "inactive" part of the channel bed. Where not otherwise specified, the parameter values used in the sensitivity analysis were  $0.2 \text{ ms}^{-1}$  for the minimum expected velocity,  $20 \text{ ms}^{-1}$  for the maximum expected velocity and a lateral resolution of  $0.5 \text{ m}$ . The distance between

the scanners was 0.79 m. The part of the sensitivity analysis aimed at finding fitting parameters for the expected velocities and for the lateral resolution was carried out on filtered data and with the wide search window (as opposed to a SW that is as wide as the IW). One parameter at a time was varied, namely maximum expected velocity ( $2 \text{ ms}^{-1}$ ,  $10 \text{ ms}^{-1}$ ,  $20 \text{ ms}^{-1}$ ,  $50 \text{ ms}^{-1}$ ), minimum expected velocity ( $0.1 \text{ ms}^{-1}$ ,  $0.2 \text{ ms}^{-1}$ ,  $0.5 \text{ ms}^{-1}$ ,  $1 \text{ ms}^{-1}$ ), and lateral resolution (0.25 m, 0.5 m, 1 m, 1.5 m and 2 m).

## 2.5 Indoor experiment

Lastly, an experimental setup to test the application was devised. The goal of these indoor tests was to investigate how reproducible velocity estimates from the LSPIV would be for a target of fixed geometry traveling at different speeds. The same pair of scanners used at Spreitgraben were fixed to the ceiling at the Geopraevent lab. The distance  $h$  from the scanners to the ground was 3.43 m and the scanners were 0.84 m apart. This corresponds to a footprint diameter and a point spacing of about 3 cm. A model debris flow was built on a wheeled platform with plastic and cardboard boxes ranging from approximately 0.15 m x 0.2 m to 0.6 m x 1.2 m, while the whole model was approximately 1.4 m x 2 m. The maximum height was 1.12 m and the model debris flow had a volume of  $1.2 \text{ m}^3$ . In an attempt to obtain repeatable velocities, a drill press was used to accelerate the cardboard model by winding up the string that was attached to the platform at well-defined rotational speeds (rpm, revolutions per minute). The diameter of the drill increases from about 2.5 cm to 3.5 cm as the string is wound up, and a mean diameter of 3 cm was used to compute the velocities depending on the rotational speeds. The resulting velocities ranged from  $1.1 \text{ ms}^{-1}$  to  $4.6 \text{ ms}^{-1}$ . Two rails were used to keep the platform in its "flow path".

After a few initial test runs, 19 runs were conducted (3–8 runs at 690 rpm, 885 rpm and 1450 rpm each). A final run at 2900 rpm ended in the destruction of the model, hence only one run was completed at that speed. For the evaluation, a maximum expected velocity of  $10 \text{ ms}^{-1}$ , minimum expected velocity of  $0.2 \text{ ms}^{-1}$ , and a lateral resolution of 0.2 m was used. Some photos from the experiment are shown in Figure 2.7.

## 2.6 Surface curvature description

The analysis of the debris-flow surface geometry constitutes an altogether different approach to extracting information from the laser data. Figure 2.8 (right) depicts a characteristic debris flow with a front higher than its tail (Costa, 1984; Iverson, 1997). As



Figure 2.7: Left: The scanners were mounted to the ceiling at a height of approximately 3.4m. Center: Front of the model debris-flow platform. The string to pull the platform is visible in the lower part of the image. Right: Top-down view of the stacked boxes simulating the coarse-grained surface of a debris-flow surge head, with the greatest height at the front. The arrow indicates the direction in which the model was pulled.

opposed to the watery tails, where particles are suspended in water, the coarse-grained fronts are sustained by grain-to-grain interaction. Measurements of pore fluid pressures at debris-flow heads show that they are essentially dry, restraining the downslope movement of the liquid tail (Iverson, 1997). That these coarse-grained fronts can also develop a convex surface, rising above the point to which they would otherwise fill the channel, has only been marginally described (Eisbacher & Clague, 1984; Colhoun, 1966). It is, however, visible in model results (Pudasaini et al., 2005), but has presumably never been measured in the field up to now. In this study, a simple approach is introduced to investigate this convex geometry, illustrated in Figure 2.8.

The approach hinges on approximating and replacing each scan line by a 4<sup>th</sup> order polynomial. Similar approaches with 2<sup>nd</sup> order polynomials have been used by geomorphologists to describe glacial troughs (Li et al., 2001; Pattyn & van Huele, 1998). Two additional steps are implemented:

**Binary identification:** The first step classifies scan lines into those that exhibit a certain amount of surface convexity and those that do not. The shape of the polynomial fit can be readily distinguished from the number of zero crossings in the polynomials' first derivative. Hence, the zero crossings are counted, and only scan lines with three zero crossings are flagged as convex. If the debris-flow channel is empty, or filled with material that does not contribute to the described convex front, the approximated polynomial forms a parabolic trough (with only a single zero-crossing). Only curves exhibiting the shape depicted in Figure 2.8 will have three zero crossings in its first derivative. Additionally, the first coefficient of the polynomial must be greater than zero. This excludes polynomials that are upside down with respect



to the expected channel geometry.

**Curvature factor:** Using the knowledge of which profile exhibits the sought-after convexity, the amount of build-up the debris-flow front exhibits is expressed in two curvature factors computed as:

$$cf_W = \frac{h}{W} \quad (2.7)$$

$$cf_H = \frac{h}{H} \quad (2.8)$$

where  $h$  is the height of the local maximum above the average height of the two minima,  $W$  is the distance between the local minima and  $H$  is the maximum flow depth of the channel.

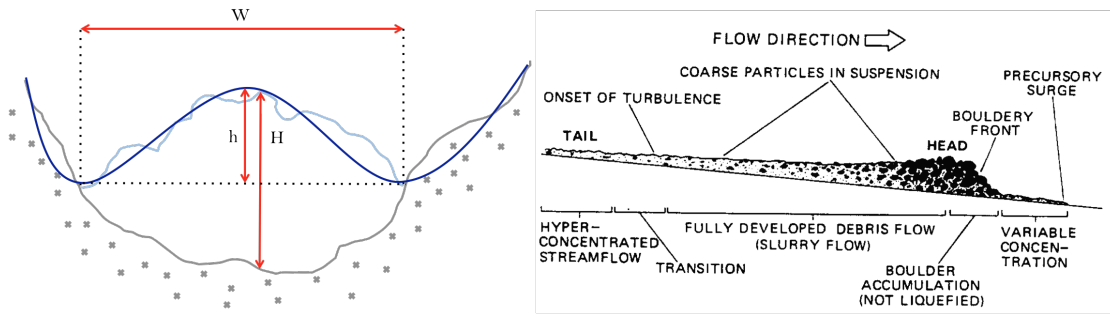


Figure 2.8: Left: Cross-flow profile of a debris flow with a convex surface (light blue line) and a best-fit 4<sup>th</sup> order polynomial (dark blue line). The red arrows indicate the measures used in Equations 2.7 and 2.8. Own illustration. Right: Longitudinal debris-flow profile illustrating the observed sorting into a coarse-grained front and a watery tail. Illustration from Pierson (1986).

Animations of sequences of profiles have proven to provide the best tool to examine the surface curvature properties of the debris flows, and a small code block is provided to export profile animations to an .avi video format.

## 2.7 Reflectance data

The scanners can also provide reflectance values for every measurement point. The reflectance value drawn from the raw data is an RSSI (Received Signal Strength Indicator) value scaled between 0 and 255. This value needs to be normalized to account for the differences in distance of the recorded pulses (Mazzarini et al., 2007). The normalized

intensity data is computed as:

$$I_{\text{norm}} = \text{RSSI} \cdot \left(\frac{d}{n}\right)^2 \quad (2.9)$$

where RSSI is the signal strength value,  $d$  is the slant range distance and  $n$  is the normalization distance. This data has not been used in the present study, but a short sequence of code was written to facilitate the extraction of this information in future studies.

## 3 Results

The sensitivity analysis and the indoor experiment constituted important steps towards a successful evaluation of the event data. The detailed results of these intermediate tests are listed in the following Sections 3.1 and 3.2, while the event results are presented in Section 3.3. Finally, the results from the surface curvature analysis are presented in Section 3.4.

### 3.1 Sensitivity analysis

Table 3.1 indicates how, as a result of the filtering, the peak flow height in event A was reduced by 0.48 m, whereas it had no effect on the flow height in dataset G. It did however slightly decrease the fraction of cells with cross-correlation velocity solutions (variable  $C_{\text{count}}$ ), by about 0.5 % in both cases.

Further runs using the filtered data revealed that enabling the quality criterion significantly lowered both the number and magnitude of measured peak velocities. For event A, 9 cells with a maximum velocity of  $19.85 \text{ ms}^{-1}$  were originally measured. This improved to only two cells with a maximum measured velocity of  $14.88 \text{ ms}^{-1}$  when applying the quality criterion. Similarly, for event G, 41 velocity outliers were measured ( $19.85 \text{ ms}^{-1}$ ) when the quality criterion was not applied, and this was reduced to  $13.23 \text{ ms}^{-1}$  (one count).

Enlarging the SW increased the number of velocity outliers slightly (6 for event A and 5 for event G), but it increased in the number of cells that yielded useable velocities from 9.8 % to 12 % and 7.7 % to 9.7 % for event A and event G, respectively.

The effects of changes to the expected velocities (defining the correlation window size) are listed in Table 3.2. Across all three events from Dorfbach, allowing for maximum flow velocities of  $50 \text{ ms}^{-1}$  led to a maximum measured flow velocity of  $19.85 \text{ ms}^{-1}$ , while  $29.78 \text{ ms}^{-1}$  resulted at the Spreitgraben. Setting the maximum expected velocity to  $10 \text{ ms}^{-1}$  or  $20 \text{ ms}^{-1}$  had no influence on peak discharge in the datasets from Dorfbach, but increased significantly at  $50 \text{ ms}^{-1}$ . For the Spreitgraben dataset, a strong increase in peak discharge is discerned when raising the maximum expected flow velocity from

$10 \text{ ms}^{-1}$  to  $20 \text{ ms}^{-1}$ . Setting the expected flow velocity to a low  $2 \text{ ms}^{-1}$  reduces peak discharge to unlikely low values, while also somewhat reducing  $C_{\text{count}}$ . Influence to mean velocity was minor in all cases.

Varying the minimum expected velocity had a large impact on all events, namely their peak discharge and  $C_{\text{count}}$ . In all cases, raising the minimum expected velocity to  $1 \text{ ms}^{-1}$  led to a distinct drop in  $C_{\text{count}}$  to values as low as 0.4% (2011), while not reaching more than 1.6% (event K). In two cases (events G and K), peak discharge reached very high values of  $168 \text{ m}^3\text{s}^{-1}$  and  $318 \text{ m}^3\text{s}^{-1}$ . This effect was less distinct for events A and M. In the latter, peak discharge was actually lowest when using a minimum velocity of  $1 \text{ ms}^{-1}$ , but the range is narrow ( $145 - 200 \text{ m}^3\text{s}^{-1}$ ). Keeping the minimum velocity at  $0.1 \text{ ms}^{-1}$  led to slightly lower peak discharges than would have been the case for  $0.2 \text{ ms}^{-1}$ , while correlation count was always highest, although this indicator must be treated with caution, since correlation windows increase in size as minimum expected velocity decreases (see Figure 2.4).

The same considerations apply to the fact that correlation count increased steadily as the lateral resolution was raised from 0.25 m to 2 m. As to be expected, peak discharge also increased slightly as lateral resolution increased, but no distinctive discontinuities were observed.

Averaging several scan lines together (see Table 3.3) in order to reduce the amount of data proved to be feasible to no more than 5 lines, beyond which  $C_{\text{count}}$  rapidly converges to zero. Thus all results from aggressively averaged datasets relied heavily on the mean velocity to compute a plausible best estimate of the total discharge ( $Q_{\text{best}}$ ), while total discharge values based solely on the values from the velocity cells ( $Q_{\text{tot}}$ ) were significantly lower.

The results of the sensitivity analysis were used to define the set of parameters used in the final processing of all available events (as specified in section 2.3.4).

Output	Event A		Event G	
	small SW unfiltered	filtered	small SW unfiltered	filtered
$H_{\max}$ [m]	2.85	2.37	3.23	3.23
$Q_{\max}$ [ $\text{m}^3\text{s}^{-1}$ ]	25.2	25.2	109	105
$Q_{\text{tot}}$ [ $\text{m}^3$ ]	785	763	1198	1219
$Q_{\text{best}}$ [ $\text{m}^3$ ]	904	887	1470	1500
$v_{\max}$ [ $\text{ms}^{-1}$ ] (#)	19.85 (8)	19.85 (9)	19.85 (44)	19.85 (41)
$v_{\min}$ [ $\text{ms}^{-1}$ ]	0.25	0.25	0.23	0.23
$v_{\text{mean}}$ [ $\text{ms}^{-1}$ ]	2.7	2.7	2.6	2.6
$C_{\text{count}}$ [%]	11.5	11.2	10.7	10.3
	small SW filtered, with criterion		small SW filtered, with criterion	
$Q_{\max}$ [ $\text{m}^3\text{s}^{-1}$ ]	25.2		35.2	
$Q_{\text{tot}}$ [ $\text{m}^3$ ]	681		567	
$Q_{\text{best}}$ [ $\text{m}^3$ ]	832		706	
$v_{\max}$ [ $\text{ms}^{-1}$ ] (#)	14.88 (2)		13.23 (1)	
$v_{\min}$ [ $\text{ms}^{-1}$ ]	0.25		0.23	
$v_{\text{mean}}$ [ $\text{ms}^{-1}$ ]	2.39		1.23	
$C_{\text{count}}$ [%]	9.8		7.7	
	filtered with large SW without crit.      with crit.		2013 filtered with large SW without crit.      with crit.	
$Q_{\max}$ [ $\text{m}^3\text{s}^{-1}$ ]	31.2	23.5	145.2	55.2
$Q_{\text{tot}}$ [ $\text{m}^3$ ]	864	718	1758	754
$Q_{\text{best}}$ [ $\text{m}^3$ ]	1013	877	1997	872
$v_{\max}$ [ $\text{ms}^{-1}$ ] (#)	19.85 (25)	14.88 (6)	19.85(69)	13.23 (5)
$v_{\min}$ [ $\text{ms}^{-1}$ ]	0.25	0.25	0.23	0.23
$v_{\text{mean}}$ [ $\text{ms}^{-1}$ ]	3.1	2.5	3.27	1.43
$C_{\text{count}}$ [%]	14.5	12	11.7	9.7

Table 3.1: Results of different processing procedures for the events A and G. The quality criterion discards correlation maxima if a minimum of 18 cells within a 5x5 neighborhood do not reach 0.7 of the maximum itself.  $H_{\max}$  denotes the maximum flow height,  $Q_{\max}$  the peak discharge,  $Q_{\text{tot}}$  the total discharge if only the cells that passed the cross-correlation criteria are considered and  $Q_{\text{best}}$  the best estimate total discharge, where discharge for the missing cells was substituted with discharge computed with the event-wide mean velocity.  $v_{\max}$ ,  $v_{\min}$  and  $v_{\text{mean}}$  describe the maximum, minimum and mean measured velocities, where the number in brackets behind  $v_{\max}$  denotes the number of cells with peak velocities. The parameter  $C_{\text{count}}$  represents the % of cells that passed the cross-correlation criteria.

Table 3.2: Results of sensitivity analysis for the cross-correlation analysis. Only one parameter was varied at a time. The default parameters were always  $20 \text{ ms}^{-1}$ ,  $0.2 \text{ ms}^{-1}$ , and  $50 \text{ cm}$  for maximum expected velocity, minimum expected velocity, and lateral resolution respectively. The cross-correlation was computed with the small search windows but applying the quality criterion.

Output	Maximum expected velocity [ $\text{ms}^{-1}$ ]			
	2	10	20	50
$Q_{\text{max}}$ [ $\text{m}^3 \text{ s}^{-1}$ ]	7.9	25.2	25.2	25.2
$v_{\text{max}}$ [ $\text{ms}^{-1}$ ]	1.92	8.50	14.88	19.85
$v_{\text{mean}}$ [ $\text{ms}^{-1}$ ]	1.07	2.33	2.39	2.51
$C_{\text{count}}$ [%]	6.0	9.6	9.7	9.8
Minimum expected velocity [ $\text{ms}^{-1}$ ]				
	0.1	0.2	0.5	1
$Q_{\text{max}}$ [ $\text{m}^3 \text{ s}^{-1}$ ]	23.88	25.2	33.4	35.5
$v_{\text{min}}$ [ $\text{ms}^{-1}$ ]	0.11	0.25	0.66	1.42
$v_{\text{mean}}$ [ $\text{ms}^{-1}$ ]	2.44	2.39	2.89	4.22
$C_{\text{count}}$ [%]	13.4	9.8	3.3	0.4
Lateral resolution [cm]				
	25	50	100	200
$Q_{\text{max}}$ [ $\text{m}^3 \text{ s}^{-1}$ ]	19.99	25.2	28.1	23.5
$v_{\text{mean}}$ [ $\text{ms}^{-1}$ ]	2.26	2.39	2.36	2.44
$C_{\text{count}}$ [%]	2.9	9.8	13.1	12.9
	14.3			
Maximum expected velocity [ $\text{ms}^{-1}$ ]				
	2	10	20	50
$Q_{\text{max}}$ [ $\text{m}^3 \text{ s}^{-1}$ ]	37.8	61.9	61.9	66.5
$v_{\text{max}}$ [ $\text{ms}^{-1}$ ]	1.89	7.94	13.23	19.85
$v_{\text{mean}}$ [ $\text{ms}^{-1}$ ]	0.93	1.51	1.69	2.01
$C_{\text{count}}$ [%]	12.0	11.7	11.3	12.8
Minimum expected velocity [ $\text{ms}^{-1}$ ]				
	0.1	0.2	0.5	1
$Q_{\text{max}}$ [ $\text{m}^3 \text{ s}^{-1}$ ]	53.3	61.9	165.73	318.02
$v_{\text{min}}$ [ $\text{ms}^{-1}$ ]	0.12	0.24	0.58	1.37
$v_{\text{mean}}$ [ $\text{ms}^{-1}$ ]	1.38	1.70	2.91	4.72
$C_{\text{count}}$ [%]	13.6	11.3	5.1	1.6
Lateral resolution [cm]				
	25	50	100	200
$Q_{\text{max}}$ [ $\text{m}^3 \text{ s}^{-1}$ ]	61.7	61.9	72.91	84.5
$v_{\text{mean}}$ [ $\text{ms}^{-1}$ ]	1.65	1.69	1.87	1.92
$C_{\text{count}}$ [%]	7.3	11.3	16.9	20.4
	23.1			

Event A				
Output	Maximum expected velocity [ $\text{ms}^{-1}$ ]			Event G
	2	10	20	
$Q_{\text{max}}$ [ $\text{m}^3 \text{ s}^{-1}$ ]	16.8	35.2	35.2	46.2
$v_{\text{max}}$ [ $\text{ms}^{-1}$ ]	1.89	7.9	13.23	19.85
$v_{\text{mean}}$ [ $\text{ms}^{-1}$ ]	0.74	1.17	1.23	1.55
$C_{\text{count}}$ [%]	7.0	7.8	7.7	7.5
Minimum expected velocity [ $\text{ms}^{-1}$ ]				
	0.1	0.2	0.5	1
$Q_{\text{max}}$ [ $\text{m}^3 \text{ s}^{-1}$ ]	20.5	35.2	176.9	168.1
$v_{\text{min}}$ [ $\text{ms}^{-1}$ ]	0.12	0.23	0.64	1.65
$v_{\text{mean}}$ [ $\text{ms}^{-1}$ ]	0.78	1.23	3.25	4.49
$C_{\text{count}}$ [%]	11.4	7.7	2.6	0.5
Lateral resolution [cm]				
	25	50	100	200
$Q_{\text{max}}$ [ $\text{m}^3 \text{ s}^{-1}$ ]	21.11	35.2	51.9	63.8
$v_{\text{mean}}$ [ $\text{ms}^{-1}$ ]	1.19	1.23	1.36	1.30
$C_{\text{count}}$ [%]	2.3	7.7	10.4	11.0
	13.2			
Maximum expected velocity [ $\text{ms}^{-1}$ ]				
	2	10	20	50
$Q_{\text{max}}$ [ $\text{m}^3 \text{ s}^{-1}$ ]	25.0	123.4	200.7	283.7
$v_{\text{max}}$ [ $\text{ms}^{-1}$ ]	1.92	8.50	14.89	29.78
$v_{\text{mean}}$ [ $\text{ms}^{-1}$ ]	0.79	4.16	4.79	5.15
$C_{\text{count}}$ [%]	2.8	3.6	3.9	3.9
Minimum expected velocity [ $\text{ms}^{-1}$ ]				
	0.1	0.2	0.5	1
$Q_{\text{max}}$ [ $\text{m}^3 \text{ s}^{-1}$ ]	151.7	200.7	167.3	144.9
$v_{\text{min}}$ [ $\text{ms}^{-1}$ ]	0.13	0.30	0.65	1.38
$v_{\text{mean}}$ [ $\text{ms}^{-1}$ ]	4.66	4.79	4.92	5.59
$C_{\text{count}}$ [%]	6.0	3.9	2.0	0.8
Lateral resolution [cm]				
	25	50	100	200
$Q_{\text{max}}$ [ $\text{m}^3 \text{ s}^{-1}$ ]	177.7	200.7	233.7	238.02
$v_{\text{mean}}$ [ $\text{ms}^{-1}$ ]	4.4	4.79	4.74	5.01
$C_{\text{count}}$ [%]	3.3	3.9	5.0	5.3
	6.8			

Event K				
Output	Maximum expected velocity [ $\text{ms}^{-1}$ ]			Event M
	2	10	20	
$Q_{\text{max}}$ [ $\text{m}^3 \text{ s}^{-1}$ ]	53.3	61.9	165.73	318.02
$v_{\text{min}}$ [ $\text{ms}^{-1}$ ]	0.12	0.24	0.58	1.37
$v_{\text{mean}}$ [ $\text{ms}^{-1}$ ]	1.38	1.70	2.91	4.72
$C_{\text{count}}$ [%]	13.6	11.3	5.1	1.6
Lateral resolution [cm]				
	25	50	100	200
$Q_{\text{max}}$ [ $\text{m}^3 \text{ s}^{-1}$ ]	61.7	61.9	72.91	84.5
$v_{\text{mean}}$ [ $\text{ms}^{-1}$ ]	1.65	1.69	1.87	1.98
$C_{\text{count}}$ [%]	7.3	11.3	16.9	23.1
	23.1			

		Number of averaged lines				
Output		3	5	15	25	75
Event A	H <sub>max</sub> [m]	2.36	2.32	2.13	2.06	2.02
	Q <sub>max</sub> [m <sup>3</sup> s <sup>-1</sup> ]	16.57	21.37	0.83	-	-
	Q <sub>best</sub> [m <sup>3</sup> ]	811	860	796	-	-
	Q <sub>tot</sub> [m <sup>3</sup> ]	355	152.5	0.65	-	-
	v <sub>max</sub> [ms <sup>-1</sup> ]	9.9	6	1.99	-	-
	v <sub>mean</sub> [ms <sup>-1</sup> ]	2.32	2.27	1.99	-	-
	C <sub>count</sub> [-] (%)	319 (5)	100 (2)	1 (0.02)	0 (-)	0 (-)
		Number of averaged lines				
		2	5	10	25	50
Event G	H <sub>max</sub> [m]	3.23	3.21	3.16	3.11	2.5
	Q <sub>max</sub> [m <sup>3</sup> s <sup>-1</sup> ]	67.9	35.2	3.9	-	-
	Q <sub>best</sub> [m <sup>3</sup> ]	786	686	355	-	-
	Q <sub>tot</sub> [m <sup>3</sup> s]	556.9	228.3	4.5	-	-
	v <sub>max</sub> [ms <sup>-1</sup> ]	9.9	3.97	0.49	-	-
	v <sub>mean</sub> [ms <sup>-1</sup> ]	1.34	1.01	0.46	-	-
	C <sub>count</sub> [-] (%)	315 (5)	53 (1)	2 (0.03)	0 (-)	0 (-)

Table 3.3: Result dependence on number of averaged lines. All other parameters were as specified in Table 3.1

## 3.2 Indoor experiment

For reasons that could not be determined, data was not recorded during the time of the main runs of the indoor experiment (or it might have been incompletely downloaded from the scanners and subsequently deleted). In any case, only the first hour of the experiment is on record, comprising the setup and a few test runs, all at 690 rpm. The experimental data revealed that the total scan angle settings on the scanners did not correspond to the settings in the *ReadOneLMSFile* function, distorting the data of the scanned area as a result. More importantly, rechecking all the processed data revealed that this was also true for most of the Dorfbach datasets, and that what had previously been identified as large amounts of noise from rain or splashing was actually an artifact of these inconsistent settings. The influence of this error can be seen in Figure 3.1. The raw data processing was subsequently repeated for all events from 2012, 2013, and 2014 (see Table 2.2).

In total, three indoor "events" were actually recorded. What is pleasing, is that the shape of the model debris flow is well distinguishable in the laser data. However, the wheels on the model debris flow were freely rotatable and the platform had the tendency to veer slightly to its orographic left, sometimes colliding with the guiding rails and losing speed. This is evidenced by the skewed and stretched appearance of the flow depth data, which

is depicted in Figure 3.2. In run 2, the rear part is very stretched, while in run 3, the rear part is compressed, indicating that velocities were not consistent between runs. The flow height computation is unambiguous, because no change of the bed can take place. In this controlled case, the absolute number of cells yielding a useable correlation is a better indicator of the quality of the velocity computation than its percentage, since the model debris flow remains the same size at roughly the same speed (hence the number of correlation cells should always be the same). The low number of velocity values computed from the second run is quite conspicuous, and the flow velocity matrix of this run actually exhibits several gaps that do not exist in the other cases. The three evaluated runs thus represent quite a variety of results, as can be seen in Table 3.4. The first run represents the ideal result, with very exact velocity and volume estimates, while all values were over- or underestimated in the other runs.

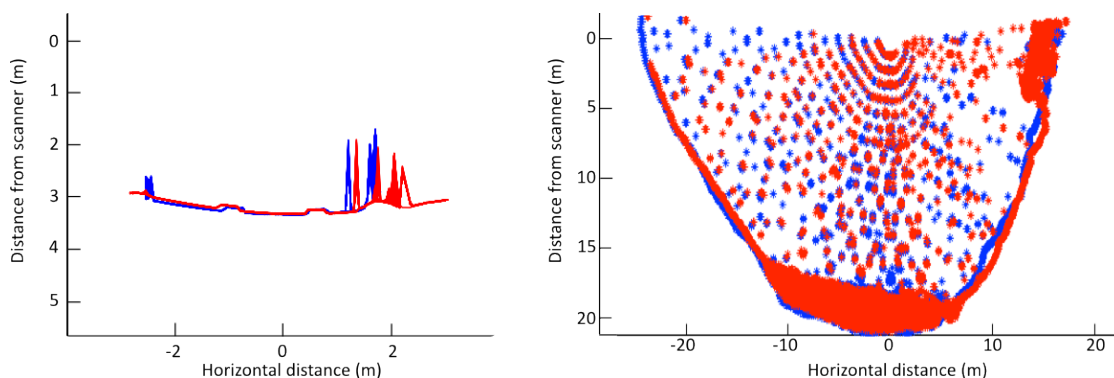


Figure 3.1: Left: Distorted flat ground beneath the scanners in the indoor experiment due to inconsistent settings. Right: Influence of the same problem on the field data at Spreitgraben. Blue and red represent the data from the upslope and the downslope scanner, respectively.

Run	Speed at 690 rmp [ms <sup>-1</sup> ]	Total dis- charge ( $\Delta V$ ) [m <sup>3</sup> ]	Peak dis- charge [m <sup>3</sup> s <sup>-1</sup> ]	H <sub>max</sub> [m]	V <sub>max</sub> [ms <sup>-1</sup> ]	V <sub>min</sub> [ms <sup>-1</sup> ]	$\sigma_{\vec{v}}$ [ms <sup>-1</sup> ]	C <sub>count</sub> [#]
1	1.1	1.2 (0)	0.7	1.13	1.07	0.77	0.10	20
2	1.1	0.7 (-0.5)	0.5	1.14	0.6	0.21	0.12	11
3	1.1	2.1 (0.9)	1.8	1.14	7.9	0.4	1.8	28

Table 3.4: Results from the indoor experiment for the three recorded runs with the model debris flow.  $\Delta V$  is the difference to the measured volume of the model debris flow.



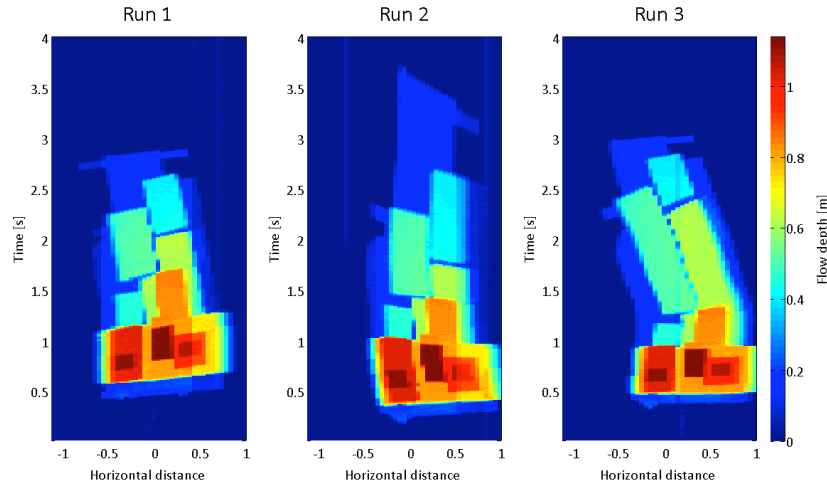


Figure 3.2: Flow depth results computed for the three runs recorded during the indoor experiment with the model debris flow built with boxes on a rolling platform.

### 3.3 Event evaluation

Events separated by several minutes or hours were treated as separate events (single letters in Figure 3.4), and in several cases, surges within the same event were also treated separately due to extensive changes to the channel bed. In this case, numbers indicate that the surges belong to the same event, and the time index is also continuous. In the present study, flow depth and flow velocities represent intermediate results, and their results are thus merely summarized in the following section. The resulting hydrographs, however, are all shown in Figures 3.5 and 3.6 on pages 35 and 36.

In total, 30 flow depth matrices were computed. In all but two cases, a pre-event and a post-event bed geometry was used to compute a flow depth. On the 11. June 2014, a first surge front (J1) stopped right below the scanner, while a second surge (J2) cleared out the whole channel a few minutes later. Due to these circumstances, flow depth for J1 was calculated with a pre-event bed geometry only, while a post-event bed geometry was used for J2. Flow depth results are spatial by nature, and since flow depth computation is fairly straightforward, the flow depth results are limited to the two examples given in Figure 3.3, while the whole set can be found in Appendix B. The events featured in Figure 3.3 illustrate the range of flow depth results and their dependence on the choice of bed geometry. While event A has three consecutive surge fronts nicely centered in the channel, event F2 shows an extreme case of levée building immediately following the passing of the first surge front, resulting in high flow depths on the orographic right side

of the talweg. This behavior is present in several other events as well (see Appendix B for details). This demonstrates how the choice of different bed geometries can result in large differences, depending on the erosion and/or deposition of material that takes place during the event. The maximum flow depth recorded for any event was 4.66 m (J2). In five cases, a flow depth larger than 3.5 m was reached, and in eight cases, flow height did not exceed 1.5 m. The lowest maximum flow depth recorded was 81 cm (F1, 2.7.2012). In 25 of the 30 cases, flow depth values in the uppermost quartile represent 2% or less of the computed values for any single event; in the remaining five cases, these represented 2% to 14% of all recorded values.

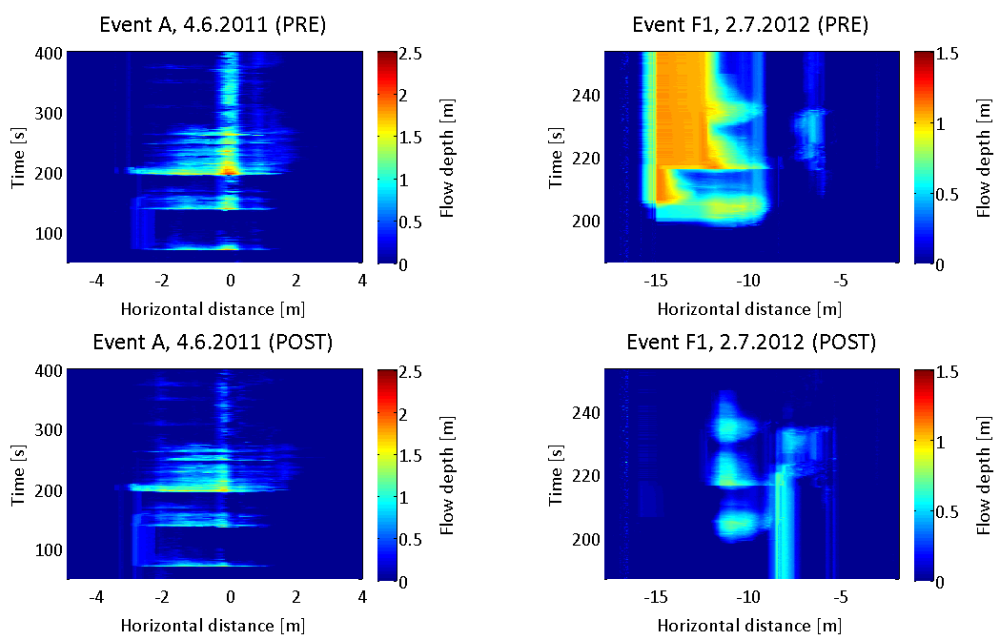


Figure 3.3: Two examples of flow depth computations with each using either a pre-event (top) or post-event (bottom) bed geometry. Differences between the two runs for event A suggest few changes to the channel bed, whereas the choice of bed geometry causes extreme changes in event F1.

Results from the flow velocity computations are summarized in Figure 3.4, while the entire collection of velocity matrices can be found in Appendix C. All the events recorded at Dorfbach feature similar velocity distributions, and differ from the event recorded at Spreitgraben (event M) which exhibits a significantly higher median velocity. The majority of events at Dorfbach (excluding C2, E, F2, H, and J1) have at least three velocity outliers. The Spreitgraben case is special, because the mean velocity was limited to

$10 \text{ ms}^{-1}$ . Typical (25th-75th percentile) velocities are  $0-2 \text{ ms}^{-1}$ , with events E and M representing exceptions to that. However, whiskers are long in some cases (notably D, E, F2, G, H, K, and M) indicating the wide range of possible velocities.

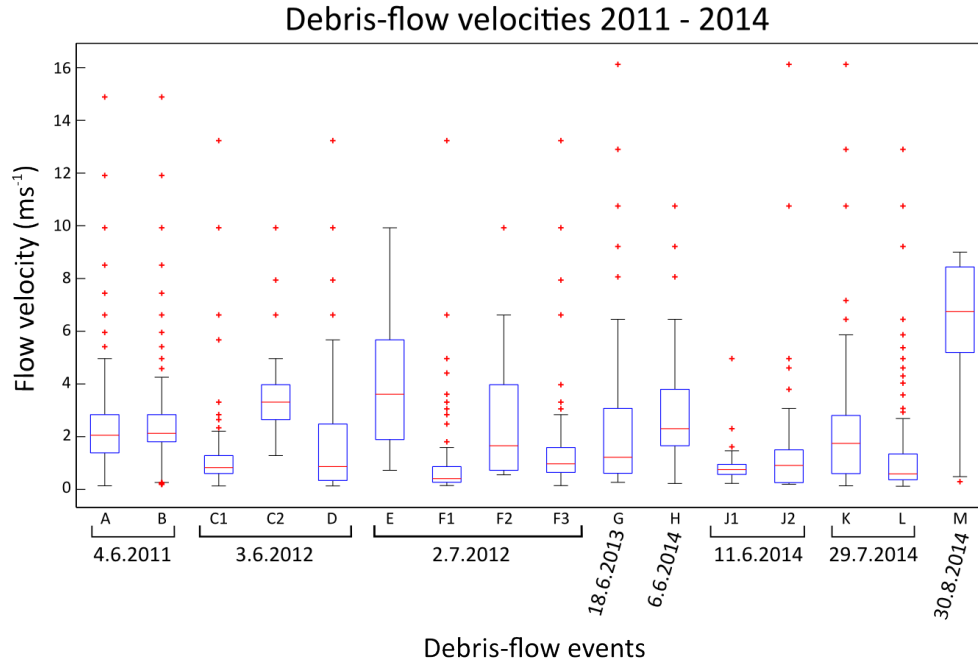


Figure 3.4: Flow velocities for all evaluated events.

The hydrographs depicted in Figures 3.5 and 3.6 reveal several distinct characteristics. For some events, notably A, B, C1 and C2, uncertainties due to channel bed changes are generally small ( $< 12\%$  of peak discharge), peak discharge values are below  $30 \text{ m}^3\text{s}^{-1}$  and the overall shape shows no extreme discontinuities. Events D, E, F2, G, and L have similarly low uncertainties due to bed changes, but the the discharge curves exhibit a much more jagged appearance, with large changes over short time periods. The opposite is the case for events K and M, where large jumps are not visible, but the use of different flow depths values induces differences of up to  $30 \text{ m}^3\text{s}^{-1}$ . Note that for event (M), the hydrograph computation of the surge front itself (seconds 480 – 540) yielded a discharge of  $2120 \pm 20 \text{ m}^3$ . For events F1, F3, and H, changes in the bed geometry result in high uncertainties, and the discharge values are highly variable. Lastly, no uncertainty range can be given for events J1 and J2, because only one flow depth estimate was computed for each event. J1 was a very small event, merely 20 seconds long before it stopped under the scanners, and discharge variability is small. J2 is characterized by a very high dis-

charge peak and a rapid decrease after that, albeit clearing the channel of all the debris that J1 had deposited.

It is evident that the described changes of the channel bed can induce very large uncertainties to the final discharge results (up to 60 % of the total volume).

### 3.4 Surface curvature analysis

Figure 3.7 shows the results obtained from the surface curvature analysis. Only events A, B, J2, and M had surfaces which the binary classification identified as convex. In the case of events A, B, and M, only the data from the upslope scanner yielded results, whereas for event J2 data from both scanners reported a surface convexity. The Spreitgraben event (M) only had a few convex profiles, but the other events manifest more sustained convex reaches. In all cases, the convex reaches are found only at debris-flow surge fronts. The results show that under the influence of the observed build-up of the debris-flow front on itself, the flow depth can increase by up to 100 % in that particular region of the debris flow. This is most evident for event J2 (both scanner datasets), where 50 % of the maximum flow height ( $cf_H$ ) is a result of the surface convexity. In the other events, the contribution is lower, typically around 20 %. Relative to the width ( $cf_W$ ) the convexity bulge is less pronounced, with most values between 5 and 10 %.

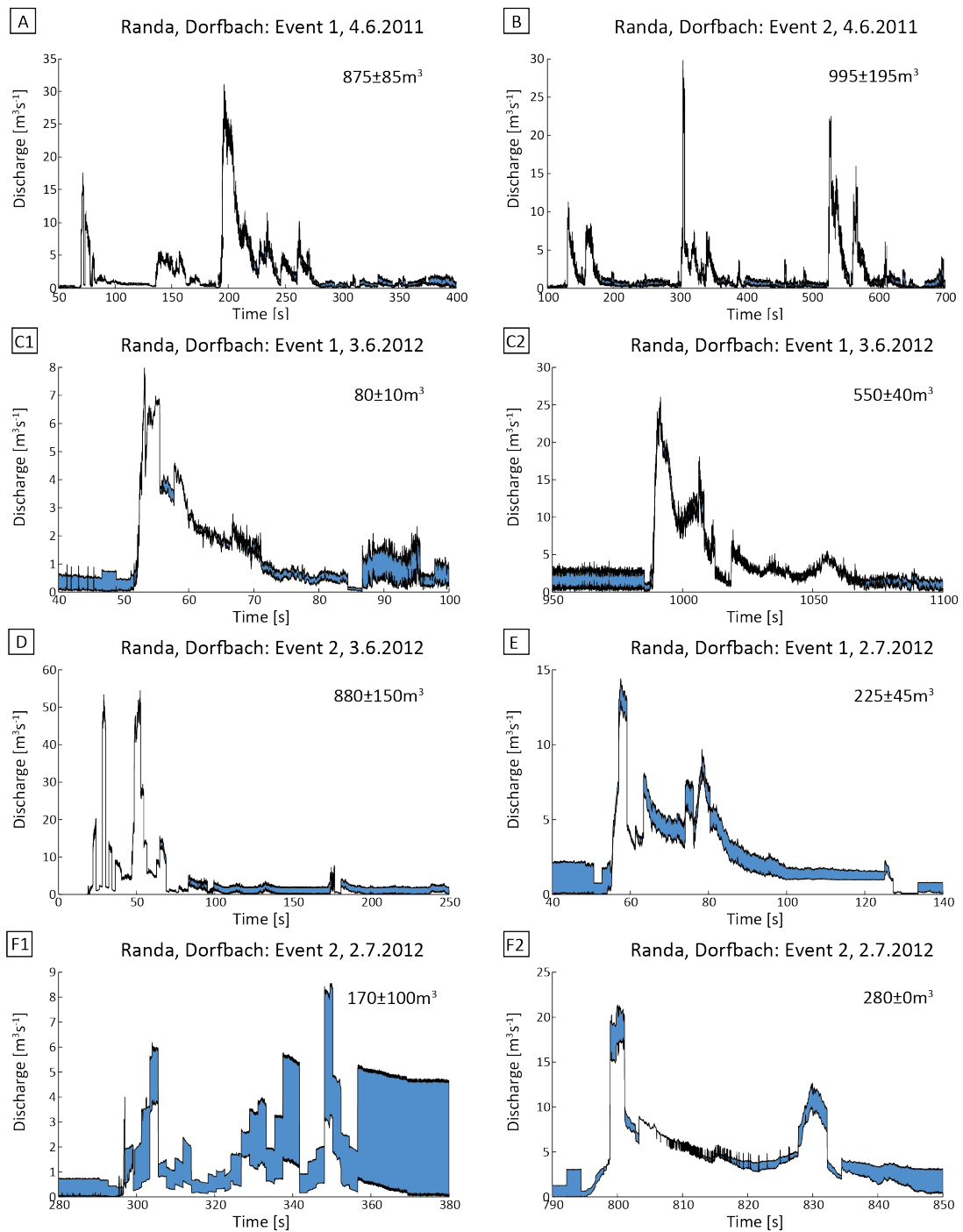


Figure 3.5: Hydrographs with approximate total discharge values. Blue areas represent the possible discharge range depending on the choice of pre- or post-event bed geometry. Note the variable scaling of the y-axis.

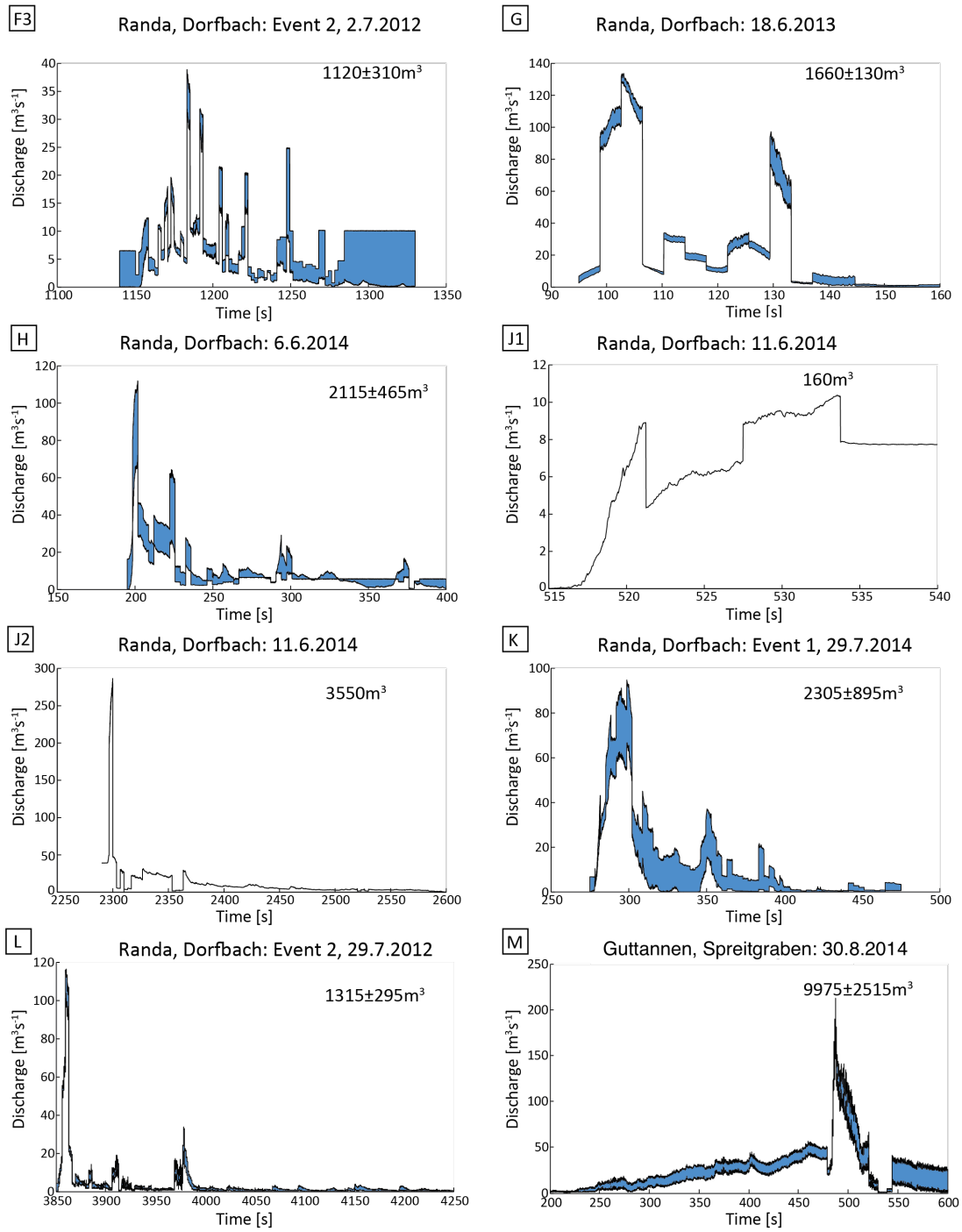


Figure 3.6: Hydrographs with approximate total discharge values. Blue areas represent the possible discharge range depending on the choice of pre- or post-event bed geometry. For J1 and J2, no range was computed because bed differences were too large. Note the variable scaling of the y-axis.

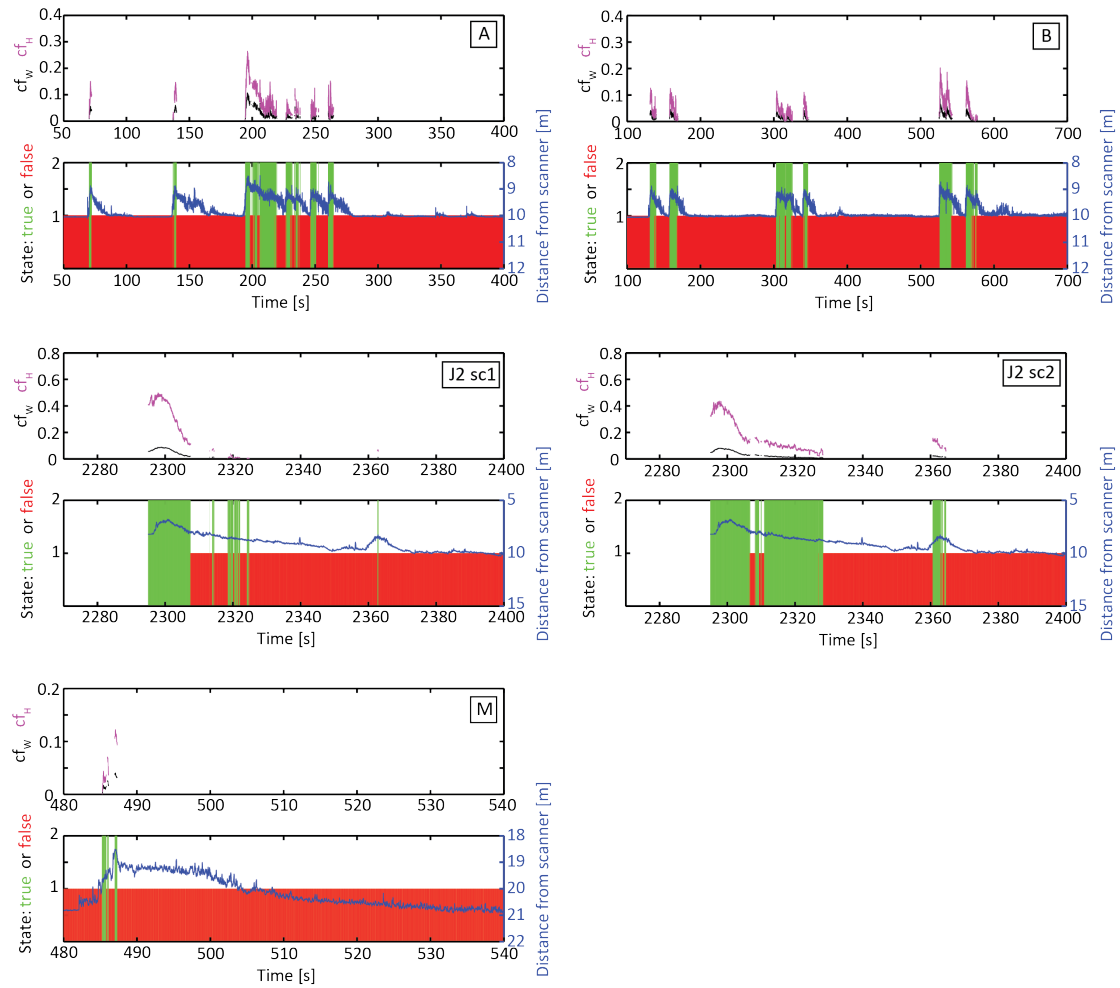


Figure 3.7: Results from surface curvature analysis for events A, B, J2 and M. In the lower half of the graphs, green areas indicate that surface convexity was detected for the individual profile line, red indicates the opposite. The blue line is an approximate center flow line to indicate where along the surge front surface convexity is detected. In the upper half of the graphs, magenta lines represent the curvature factor  $cf_H$  and black lines represent the curvature factor  $cf_W$ .





## 4 Discussion

The main focus of this study was to assess the computability of the principle debris-flow variables from the laser scanner data in an automated or semi-automated way, and to supply a code package that can be used to do the same in future studies. In addition, the uncertainties of the method and the sensitivity of the output to processing parameters were investigated. The study has shown how *flow depth*, *flow velocities*, *total discharge* and *peak discharge* can be computed in a relatively straightforward manner from a novel application of the LSPIV approach to concatenated laser profiles.

Sections 4.1 through 4.6 are aimed at answering the primary research question (1) and its associated subordinate questions (1.1–1.3), as formulated on page 5. The uncertainties arising from each of the different processing steps are discussed individually in sections 4.3 through 4.6.

As stated in research questions 2 and 3, a second goal of the present study was to investigate the possibility of describing the surface geometry of debris flows with regard to their cross-flow convexity. These findings are discussed in section 4.7.

Lastly, section 4.8 discusses the possibilities and limitations of such a setup with regard to the use in operational debris-flow warning systems.

### 4.1 Sensitivity analysis

Prior to performing the final runs with all the datasets recorded by the scanners, the developed methodology was evaluated in a sensitivity analysis, aimed at finding one set of parameters that could be used in the processing of all events.

Given the fact that only two datasets were used to test the effect of filtering, the quality criterion and the size of the SW, and that this number was only raised to four datasets to evaluate the influence of the processing variables, it must be recognized that the explanatory power of the performed sensitivity analysis is limited. An analysis of this sample size will not reveal statistically significant results. In most cases however, the observed effects were similar, so useful insight was gained.

That the filtering did not have an effect on flow height is a good sign if it is assumed that

no splashes were removed where none exist. Visual inspection of dataset G does indeed suggest that the surface of that particular debris flow was very smooth. On the other hand, splashes are clearly identifiable in dataset A, and these are efficiently removed by the filter, reducing maximum flow height. However, maximum flow depth is not necessarily a good indicator of filtering performance because the spatial variability of flow depth can be large and visual inspection can only reveal the very obvious changes. The sensitivity analysis also found that the number of cross-correlation cells with velocity solutions identified in dataset G is slightly lower when working with the filtered data. It is however impossible to discern whether this reduction is due to the loss of some valuable surface information, or the removal of cross-correlation maxima that were based on random splashes producing erroneous cross-correlation peaks.

The results of the sensitivity analysis indicate that a large SW, combined with the implemented quality criterion, constitute an improvement in the processing. This statement is based on the assumption that the highest detected velocities of  $19.85 \text{ ms}^{-1}$  were erroneous. This cannot be known for certain, but observations at Dorfbach (Graf et al., 2013) and common velocity values found in the literature suggest that the majority of observed debris-flow velocities are lower than  $15 \text{ ms}^{-1}$  (Hürlimann et al., 2008; Prochaska et al., 2008; Toyos & Gunasekera, 2008; Arattano & Marchi, 2005; Hürlimann et al., 2003; Marchi et al., 2002; Genevois et al., 2001; Arattano & Marchi, 2000; Arattano & Grattoni, 2000; Rickenmann, 1999; Costa, 1984).

The statements related to the size of the SW by Meunier & Leweke (2003), Raffel et al. (2007), and Hu et al. (1998) are all based on the PIV methodology applied to time-lapse imagery, and translating these requirements to the problem at hand is not a straightforward task. Since particle sizes can vary strongly in debris flows, following Meunier & Leweke (2003) to incorporate at least four, but preferably more particles within an IW would possibly call for larger lateral resolutions. This would however degrade the representation of varying velocity fields in the cross-flow direction. In the temporal dimension however, the particle amount is strongly dependent on the actual flow velocities. High flow velocities will cause more particles to be present in one window, but they also compress the representation of the single particles in the temporal direction, possibly making them harder to identify. The relationship between the size of the IW and that of the SW might be slightly more straightforward in debris flows than it is in rivers, where particles are more likely to move upriver due to eddies. Assuming that no significant deceleration takes place between the two scanners, there is no need to make the SW longer than the IW if the offset between the time index of the two datasets is correct. Logic dictates that the spatial (cross-flow) width of the SW should be in the range of the expected lateral

movement of a particle between the scanners, though this is not easy to identify. More research is needed to identify the ideal dimensions of the IW and the SW for use with concatenated laser profiles.

The performance of the PIV step is closely tied to the relations between lateral resolution, window length (a dependent variable of minimum expected velocity) and the grain size distribution and flow speed of the event. The use of  $0.1 \text{ ms}^{-1}$  as minimum expected velocity should provide enough time for slow objects to be fully captured in the IW and SW, and thus be distinguished in the high pass filtered surface. The sensitivity analysis also revealed a direct relationship between lateral resolution and peak discharge. This can be explained by the fact that a wider velocity cell is more likely to coincide with high flow depths values, thus augmenting peak discharge values. More extensive sensitivity studies would be needed to better understand these relationships, and to decide whether adaptive grid sizes that have been used in photographic PIV also have the potential to improve the laser versio (Theunissen et al., 2010, 2007).

It is possible that the best results will only be achieved by tuning processing parameters for each event, rather than expecting one set of parameters to work uniformly. This said, working only with field data will make it to ascertain LSPIV performance, unless video data is fully exploited or large-scale flume experiments can be incorporated.

The implemented quality criterion is a very basic one. Many different ways of dealing with velocity outliers have been suggested, commonly using some kind of filtering or smoothing technique (Dobson et al., 2014; Travelletti et al., 2014; Zhang et al., 2013; Stanislas et al., 2008; Meunier & Leweke, 2003; Holland et al., 2001). Especially in riverine environments and when using seed particles, the velocity field is generally much larger (i.e. many more single vectors), and the filtering of velocity outliers becomes easier. It is hard to estimate just how good the implemented quality criterion actually is, (beyond that it seems to work well), and a more in depth investigation of this topic is necessary.

## 4.2 Indoor experiment

The main goal of the laboratory experiment was to assess the processing workflow in more constrained conditions with known object size and speed. This objective was reached, as the experiment revealed the errors induced by the described settings inconsistencies. Due to the fact that the majority of the data was lost before it could be evaluated, it was not possible to carry out an in depth analysis of speed and discharge results.

The flow depths of runs 2 and 3 (Figure 3.2) suggest that they were influenced by the

breaking effect of the rails and the rotating of the wheelboard. Theoretically, assuming that the velocities are always measured correctly, these effects should not have an impact on the final discharge. At the cells in run 2 for which no velocity could be computed, mean velocity for that scan line was used to compute discharge, albeit not improving the result significantly. This suggests that any gain from using the mean velocity to fill gaps in the hydrograph depends strongly on the quality of the overall velocity estimates. Run 1, however, shows that the applied method can successfully determine the correct discharge. However, it is hard to draw concrete conclusions from this small experiment; many more runs would need to be evaluated. Also, differences in scale should be considered - a stack of boxes cannot compare to a real debris flow. In the indoor experiment, the laser footprint was significantly smaller than the smallest object, while these are expected to be more similar in the field. Due to the size of the correlation windows in relation to the size of the "debris flow", the influence of a few wrong velocity estimates has a much larger influence on the final discharge value. This is assumed to be the main reason for the erroneous results of runs 2 and 3. Further tests with different dimensions of the IW and the SW could shed light on these relationships and what the ideal dimensions should be. However, given that the model debris flow was a solid object (and should appear identical, aside from some skewing, in both scanners) it is concerning that the difference in the cross-correlation performance between the runs was fairly large.

The indoor experiment raises a few concerns, but viewing this experiment as a precursory trial for a larger scale validation, some conclusions can be drawn: Video recordings of all the runs would facilitate explaining the differences in the results. Accelerating a wheeled platform with a drill press is certainly not a state-of-the-art method, and a more controlled setup would be desirable. A serious experiment would undoubtedly also need to be set up at a larger scale more like that of a real debris flow. And, as mentioned under point 4.1, significant velocity changes right between the scanners are problematic, but might have taken place in this particular setup due to collisions with the guiding rails.

### **4.3 Raw data: errors, interpolation, and filtering**

The settings inconsistency discovered with the indoor experiment (Figure 3.2) accounted for most of what had previously been interpreted as noise from rain or water dripping off the platform. The problem was found to lie in the fact that the start and end angle settings of the scanners need to be set manually in the function *ReadOneLMSFile*. Based on this angular range, and the number of points in each scan line (which is read from the

scanner raw data file), the angle vector is calculated. If the number of points does not correspond to the number of angle steps between the start and end angle, the angle vector will be, albeit only slightly, incorrect. This causes large errors (see Figure 3.1) when the data is transformed from the polar to the cartesian coordinate system. The effect of this error was much more dramatic in the field than it was for the indoor experiment, where it caused only a slight distortion of the data. The extent of this difference is surprising and not entirely clear. Adding a simple check to the *ReadOneLMSFile* function, or modifying the scanner settings to write the start and end angles into the output file, would be straightforward options to avoiding this problem in the future. The problem also goes to illustrate the importance of a well-documented field setup.

Apart from this, the raw data does contain some points which are assumed to be erroneous file values or measurements (e.g. zeros and non-hexadecimal values, measurements anomalously close to the scanners). Excluding points that are below a minimum threshold distance defined in the *ReadLMSFiles* function gets rid of most erroneous measurements, so that these do not provide an earnest source of error. Occasionally, points are projected below the channel bed, but these do not influence the final result as they are isolated occurrences and are averaged out in the computation of the bed geometry.

The fact that the scanners are suspended from cables above the channel makes them susceptible to wind-induced motion. At Spreitgraben, the scanner platform is weighted down with stones in the hopes of minimizing motion. Based on the way that the platform is suspended with two cables (Figure 2.1), roll, pitch and yaw of the platform itself are not expected to dominate, unless in severe storm. But it must be recognized that little movement is needed to disrupt the scan pattern, and lighter winds could cause vertical motion of the platform. It is presumed that platform movement would be detectable in the range of measurements along the banks of the channels. Assuming that these are stable, the standard deviation of distance values in the raw data should be small over these areas. Across all datasets and for the first six readings at each end of the scanners range, mean standard deviation of the raw distance from the scanners is 12 mm. Based on the available images and video recordings of some of the observed events at Dorfbach, this is estimated to be at least one order of magnitude smaller than the surface roughness. This issue has, however, not been investigated in detail, and effects such as the ones visible in the flow depth data of event F1 (see Figure 3.3) raise questions about inaccuracies possibly stemming from scanner motion. It is possible that scanner motion could be estimated from the data itself, but due to constant changes of the bed, placing an inertial measurement unit on the scanner platform would likely provide more reliable results. Otherwise, a fixed stable area under the scanner would be necessary, and even

from that, defining the direction of platform movement could prove difficult.

It must be assumed that the way objects are mapped by the scanners defines the performance of the LSPIV algorithm. The effect of averaging depending on the relation between  $d_p$  and  $D_s$  is expected to be marginal since all values are interpolated onto a regularly spaced grid using linear interpolation, and this is assumed to have a much larger effect on the smoothing of the surface. Further investigations of this topic can yield insight into the algorithm performance as a function of line and point averaging (see also Figure 4.3), and even whether interpolating the data to a regularly spaced grid is optimal (beyond for computational efficiency of the processing).

Depending on levée building and flow path, parts of the channel can sometimes be obscured from the scanner. This effect is especially prominent in some of the 2012 events. Due to the interpolation onto a regular grid that is performed once the raw data has been transformed into the cartesian coordinate system (section 2.3.1), this missing information can be replaced to some extent. However, the interpolated surface is constructed by linearly interpolating between the nearest visible points, usually somewhere on the other side of the levée or channel, and clearly does not represent the real surface adequately (see Figure 4.1). Using linear interpolation makes sense for areas that are completely obscured. It would also be possible to use a more sophisticated interpolation technique that also respects neighboring values through time, but it is not clear that this would provide a significant improvement. For areas on the surface of the debris flow however, a nearest neighbor interpolation might provide better results with regard to preserving as much of the surface roughness as possible. Both issues are considered to have marginal effects on the final discharge estimate, but the influence on the cross-correlation analysis is unclear and should be further investigated. Clearly, where the linear extrapolation is calculated across larger areas, no valid cross-correlation match will be found. It might even produce false results, if a similar extrapolation is conducted in the datasets of both scanners. Features resembling "ripples" are visible in Figure 4.1. If both datasets exhibit these, false cross-correlations might be detected.

## 4.4 Bed geometry and flow depth computation

Changes in the bed geometry during an event are the greatest source of uncertainty with regard to the final discharge results. That these changes can be very large, and that both erosion and deposition can take place during a single event is evident in the laser datasets, and has also been shown by other studies (Berger et al., 2010; Hungr et al., 2008). An

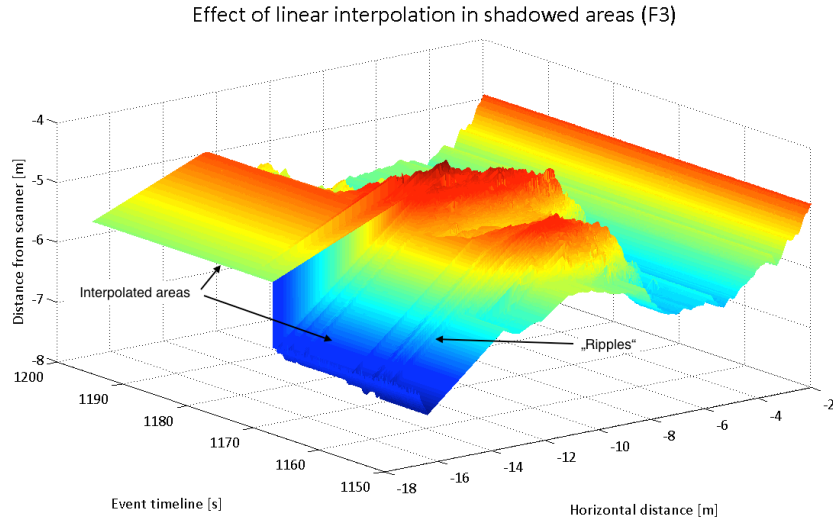


Figure 4.1: Effect of linearly interpolating areas shadowed by levées or the surge front in the case of event F3. The orographic right channel bank has been removed in order to more clearly see the debris-flow surface.

extreme example of bed changes during a single event is given in Figure 4.2, where the bed level along the central flow line changes at least five times. Using a static bed-geometry for the entire duration of the debris flow is therefore very unrealistic, and this can only be partly counteracted by computing a second bed-geometry following the event. It is however a simple and effective way of estimating the influence of bed changes on any single event. An improvement would be to define multiple bed-geometries throughout the debris-flow event. This could be done manually, or where clear surge fronts are identifiable, even automatically, based on the identification of a rapid decrease of the distance to the scanner across large portions of the channel. This improvement would come at higher computational costs, and the benefit of it would have to be investigated in detail. Where flow depth rises more gradually, and the channel is filled with water and sediment prior to the passing of a surge front, the definition of a bed-geometry and the subsequent flow depth computation remain difficult. It must be stated however, that this problem is inherent to any computation of debris-flow discharge (Marchi & D'Agostino, 2004; Hürlimann et al., 2003). Yet, in contrast to the established methods of using radar or ultrasonic gauges (Itakura et al., 2005), the laser profile scanners offer unprecedented accuracy for quantifying spatio-temporal changes of the channel bed below the scanner position. Additionally, where changes of flow path occur, the large coverage of the scanners provides a distinct advantage over radar or ultrasonic gauges that need

to be centered over the channel.

A further issue is introduced by the flow depth computation method. Equation 2.3 does not allow for negative flow height because this was not regarded physically possible. Due to this, whenever a debris-flow erodes its bed to a deeper stage than that prior to the event, all flow over that area is disregarded or underestimated. This is especially problematic when the debris flows over a bed that consists entirely of previously deposited debris and sediment, as was most prominently the case in 2012 at Dorfbach. On the other hand, where levées are deposited, flow depth is detected where none exists, contributing to significant areas of overestimated flow (see Figure 3.3). Ideally, the channel bed under the scanners would be artificial or bedrock to prevent erosion, and steep enough to prevent deposition.

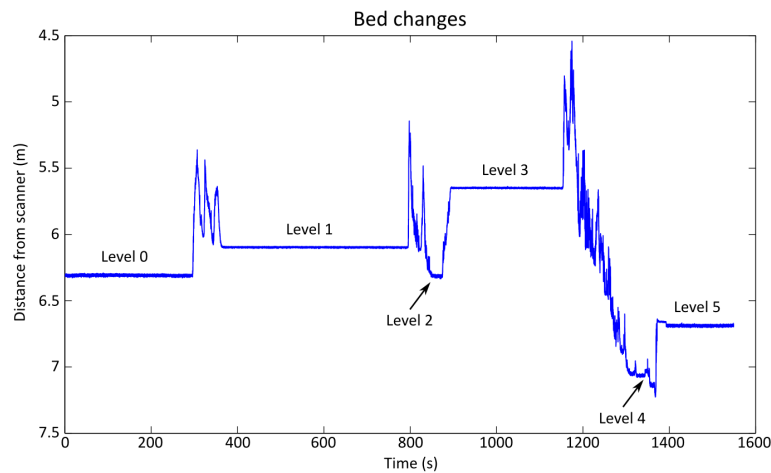


Figure 4.2: Longitudinal profile of event F (surges F1–F3) showing extreme changes of the channel bed along an approximate central flow line. All three surges were processed separately, to reduce the influence of the bed changes. The levels are not necessarily the lowest points in the bed, but the thalweg changed little throughout the whole event.

## 4.5 Displacement analysis using LSPIV

Determining flow velocities using an (LS)PIV approach has proven successful in numerous hydraulic applications (Dobson et al., 2014; Zhang et al., 2013; Le Coz et al., 2010; Muste et al., 2008; Fujita et al., 1998), and the same method has been applied to TLS data, albeit for much slower processes (Kenner et al., 2014; Aryal et al., 2012). Applying this approach to concatenated laser profiles, however, constitutes a novel application. Based



on the available data, a satisfactory validation of the computed velocities is not possible. The fact that velocity estimates are, for the most part, within a reasonable range, and also that in one run of the experimental setup the measured velocities equaled the expected velocity, suggest that the majority of the velocity computations are correct. Additionally, regions with cross-correlation values that are above the minimum cross-correlation threshold and that pass the quality criterion are persistently identified at the debris-flow fronts and slightly behind them, not during sequences where the channel is empty or water flow is expected. This indicates that the cross-correlation works in areas where the surface is in fact in motion and the roughness is high enough for a displacement to be identified. Furthermore, comparison of the velocities recorded the individual events (Figure 3.4) revealed a significant difference between Spreitgraben and Dorfbach. Although it is hard to base this statement on one single event, such a difference would have been expected based on events previously observed at the two sites (Graf et al., 2013; Tobler et al., 2012).

It must be recognized that the computed velocities represent point velocities that are derived from cross-correlation maxima caused by single objects, presumably rocks transported on the surface of the debris flow. These point velocities are then applied to the entire cell, whose size is defined by the lateral resolution and the minimum expected velocity. This may lead to overestimating peak discharge in some cases, since a point velocity, say a boulder rolling down a surge front, influences a large area that is more likely to coincide with areas of high flow depth. Although not applied to debris flows, Dobson et al. (2014) use a Gaussian interpolation considering neighboring values to compute a sub-pixel interpolation of the velocity matrix. Introducing such a smoothing step could significantly reduce the influence of isolated high velocity estimates and maybe provide more reliable peak discharge values.

Central to the computation of the flow velocities is the distance between the scanners, a measurement that can easily be determined directly from the scanner platform. However, this distance was changed when the scanners were tilted away from each other by  $1.5^\circ$  in 2013. This causes the distance between the scan lines to become a function of the fixed distance between the scanners and the variable height of the debris flow surface. A change in height of 1 m results in only a 2% velocity change, which is not considered significant for the final discharge estimate. Similar considerations apply to flow which is not perpendicular to the scan lines. These issues raise the question as to what the ideal distance between the scanners should be, to prevent too much change at the debris flow surface while keeping the distance large enough for a reliable velocity estimate. The numbers in Table 2.2 show how large the influence of scanner tilting can be.

In terms of the range of velocities recorded, event J1 clearly stands out from the rest. This event was recorded on video and is known to have been very slow, to the point that it stopped under the scanners. The flow depth measurement for this event shows a very clear structure of boulders at the surface. The following event (J2) cleared the entire channel of debris almost instantly, presumably running into the deposited debris at high speed. Comparing an identical subset of the J2 flow depth shows a much less clearly defined picture of the debris flow surface. The comparison depicted in Figure 4.3 raises the question as to how well the cross-correlation performs in these different cases. On a related note, due to the large bed changes that can occur across very short distances, scanner views may differ substantially. This is especially pronounced in the 2011 datasets, where a large overdeepening formed below the downriver scanner. This did not, however, lead to a degradation of the cross-correlation analysis. Further research is needed to understand what circumstances dictate the performance of the LSPIV in such cases.

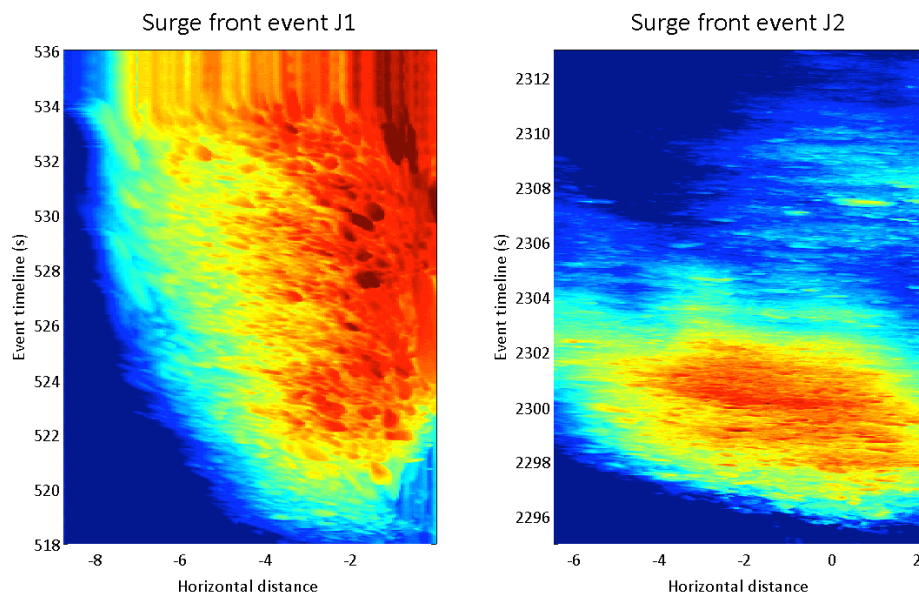


Figure 4.3: The mapping of the surge fronts is heavily speed dependent, as can be seen in the images above. J1 was a very slow event, to the point that it stopped below the scanners. J2 on the other hand cleared all the debris deposited by J1, presumably crashing into the latter at high speed. The images are distinctly different, even though they are of equal dimension, and raise questions about cross-correlation performance. Blue to red colors depict the transition from low to high flow depth.

The performance of the high-pass filter implemented in the LSPIV algorithm has not been investigated in this study. This is an evident future task since the quality of the surface used in the cross-correlation defines the performance of the displacement analysis. Entirely different approaches to the velocity computation are also conceivable: Schubert et al. (2013) applied a multi-scale wavelet based approach to SAR (Synthetic Aperture Radar) data to determine glacier motion. This approach provides a field of sub-pixel displacement estimates, thus reducing the influence of sparse, isolated velocity measurements, but they have found cross-correlation to provide slightly more reliable estimates. Alternatively, a scale dependent feature detection (Lindeberg, 1998) of objects at the surface of the debris flow could provide a starting point for either pixel-by-pixel or cross-correlation based displacement analyses. Regardless of the chosen method, there are some unavoidable challenges inherent to this dataset. The mapped objects move very quickly, they can rotate, become submerged, or shatter apart as they travel between the two scanners, and different objects can look very similar imaged as height profiles. Any chosen approach can only be as good as its capacity to deal with these problems.

## 4.6 Hydrograph generation

Generating hydrographs for each event is a technically straightforward task once the flow depth and the flow velocities are known. One source of error introduced by the processing is the velocity extrapolation to areas where no velocity was measured by cross-correlation. The linear extrapolation used does not mirror the complex, non-linear relationship between flow height and flow velocity (Prochaska et al., 2008; Rickenmann, 1999; Iverson, 1997). However, in absence of any other known parameters describing flow characteristics, using the median flow velocity along every cross-flow line, is a feasible approximation, as it respects velocity gradients that have been observed throughout the duration of debris flows (Arattano & Marchi, 2000). However, this strategy can be problematic where flow is narrowly channelized. As the number of cross-flow velocity cells is a function of the chosen lateral resolution, velocity extrapolation may be based on a very small number of observations. Additionally, wherever levée deposits were misidentified as flow depth, discharge values will be computed there as long as at least one velocity estimate exists along that cross-flow profile, further amplifying the errors introduced by deposition processes. It might be preferable to use an overall median or mean velocity for profile lines with fewer than a certain number of cells with velocity solutions, much in the way that the empty lines are currently filled with the overall mean velocity. It's beyond the scope of this thesis to discuss every hydrograph individually. Alterna-

tively, some common characteristics and particularities are pointed out. Peak discharge is likely to be overestimated in many cases because the influence of the velocity cells is large while regions of peak flow height are usually small. It is presumed that the accuracy of the final discharge volume is primarily dependent on the magnitude of the changes to the bed, and that the precision of the laser height measurements have no influence on the result. The filled blue range between the two estimates plotted in Figures 3.5 and 3.6 emphasizes this. It must be noted, however, that the boundaries of this range, representing a choice of pre- and post-event bed geometries for computing flow depth, are not necessarily representative of the full uncertainty (mid-event bed changes could be contributing additional error). Although the 2011 location of the Dorfbach scanners was criticized for being above a steep slope, over which debris flows tended to accelerate (pers. comm. C. Graf), the results suggest that this might indeed have been the best location. The steeper slope reduced debris deposition, and the 2011 event has the narrowest uncertainty range of all events. Many of the later events exhibit significant bed changes and suffer from correspondingly large uncertainties.

Due to the scarcity of validation data, a comparison to the results presented here is hardly considered meaningful. Differences in data acquisition makes comparison difficult, and drawing conclusions from only two events would be misleading. What can be stated, is that the maximum depth derived from the laser data is higher than that derived from the radar data. This is expected since the radar sensor averages over a much wider field of view, missing extrema "visible" to the laser scanners. With regard to discharge, stating anything more precise than that both methods yield similar magnitudes is considered misleading.

Dorfbach events are mostly small to medium in size (no more than a few thousand  $\text{m}^3$ ), with events of June and July 2014 representing the largest events recorded in the last four years. What is remarkable about this dataset is the fact that a discharge estimate could be computed for every single event. This constitutes a significant improvement over the established setup, where the velocity computation is strongly dependent on the (very variable) quality of the geophone readings, and only two events could be evaluated. With regard to all the previous events recorded at Spreitgraben, the 2014 event is hardly worth mentioning. After two eventless summers however, it goes to show that events can still be expected any time at Spreitgraben, albeit possibly at smaller magnitudes than those experienced 2009 through 2011.

## 4.7 Surface curvature

The surface convexity detection and parametrization presented in this study are the first of their kind. Although curve fitting has long since been applied to describe glacial valley cross sections (Li et al., 2001; Pattyn & van Huele, 1998; Graf, 1970; Svensson, 1958), the surface geometries of debris-flow surge fronts have not been investigated and measured in this way. It is assumed that the formation of a convex surface is an immediate consequence of the internal dynamics of the debris flow and its grain size distribution, or "rheology" (Iverson et al., 2010; Iverson, 2003, 1997; Costa, 1984). The laser scanner dataset appears to provide the information necessary for this kind of analysis, and it has yet to be established which parameterizations prove most useful.

The major shortcoming in the current method is that only the polynomials are analyzed. In order to come to more reliable conclusions about the shape of the surface throughout a debris-flow event, the extrema identified on the polynomials could be used to find the corresponding maximum and minimum in the original data. The absolute range of values computed might well be artifacts of the method applied, and more research is needed to understand the benefits and constraints of the selected approach. Visual inspection of some of these fitted curves suggests that the height of the maximum is often underestimated, while the minima are often overestimated. In some cases when a convexity was readily identifiable to the unaided eye (e.g. Figure 4.1), the proposed algorithm nevertheless failed to identify the phenomenon. These errors were due to the geometric structure of the channel being complicated by deposited levées, so a more flexible approach is needed.

Although the results presented in this thesis provide only a quantitative glimpse into the relationships between  $cf_H$ ,  $cf_W$ , flow depth and debris-flow progression, it is instructive to compare different surges of the same event. The results suggest that curvature factors also depend on channel geometry, but the number of analyzed events is too small to come to more definite conclusions about this relation. Alternatively, Hungr (2000) hypothesized that pronounced debris-flow heads take time to mature. This could explain why surface convexity was not found for all events.

The curvature factor  $cf_H$  suggests that up to 50% of the total flow depth can come from the formation of the convex surface geometry. This is based on the assumption that the maximal curvature is reached at the place of the highest flow depth, which is not necessarily true. However, these results indicate that post-event mudline observations in debris-flow channels may not always be reliable indicators of maximum flow depth. The fact that surface convexity persistently detected at the surge heads suggests that

the surface curvature can be used as a proxy of the longitudinal rheology, indicating the transition between the bouldery front and the watery tail of a debris flow. Many more such measurements will be needed to establish the nature of the connection between curvature and the debris-flow rheology.

Therefore it is possible to describe and quantify the surface curvature of a debris flow from the measurements obtained with the laser scanners (research question 2 and 3), although it has yet to be seen how robust the results are and how the method may be improved. A comparison of the surface curvature to the number of impulses recorded by the geophones could also yield interesting clues about the relation between curvature and grain size (part 2 of research question 3), which cannot as yet be answered satisfyingly. It is believed that a better understanding, description and quantification of this characteristic trait of debris flows should prove interesting to a large scientific community.

## 4.8 Operational value

The scanners would be a valuable addition to operational monitoring and warning systems (especially in wide channels where radar or ultrasonic gauges can miss the passing of a debris flow) while also providing accurate and distributed flow height measurements. In such applications, one scanner may be sufficient if an estimate of velocity can be derived by other means (Osaka et al., 2013). One scanner can still provide important data for research projects aimed at understanding the geometric characteristics of debris flows, bed changes and levée building properties. The velocity computation requires at least two scanners, but they provide distinct advantages over geophones since the feasibility of the velocity computation does not depend on the subsurface at the location of the scanner or its distance to the debris flow (Hürlimann et al., 2003). For a given channel, ideally with an artificial bed, it would technically be possible to compute peak flow depth, flow velocities, peak and total discharge fully automatically. In an operational field warning system the foremost limitation is computational power (indirectly limited through electrical power availability). On a modern computer (3 GHz Intel Core i7 processor, 16GB 1600 MHz DDR3 RAM memory), reading one hour of raw data takes 15 minutes. Once the raw data has been read to memory for analysis, all values could be available within 30 minutes. The better an event can be isolated, both in time and cross-flow distance, the more efficient such an evaluation would be. As such, an ideal monitoring location would have a narrow, artificial bed steep enough such that the deposition of debris is impeded. Furthermore, assuming that computational infrastructure is not available on site, excellent data transfer rates would be necessary to transmit the data to a lab. A

real-time evaluation seems unlikely at this point, but estimates can be available within a reasonably short time. Alternatively, the temporal resolution of the scanners would have to be reduced, but the sensitivity analysis did not suggest that this would yield useable velocity (and thus discharge) measurements. What does seem entirely feasible is extracting only distance values in real-time, and these could be used to detect a debris flow. The SICK standard software could be used for this, and possibly other tasks as well, but this has not been looked into.

It must be stressed that this work is regarded as a single case study, with most events exhibiting similar characteristics. Based on the results from the displacement computation presented in this study and the understanding of the LSPIV functionality, it is likely that the monitored debris-flows need to exhibit a certain amount of granularity for the cross-correlation to yield useable results. This would limit the applicability of the lasers to a certain range of events. This said, it must again be emphasized, that no recorded debris-flow event has gone unevaluated, which constitutes a significant advantage over the established system.





## 5 Conclusion

This study provides a first assessment of the potential of data obtained from two vertical laser profile scanners, mounted above a debris-flow channel, for deriving the principle debris-flow characteristics *flow depth*, *flow velocities*, *peak discharge* and *total discharge*. The established method of large-scale PIV was applied to the concatenated laser profiles, and the results indicate that the instrumental design and data processing permits the extraction of the aforementioned variables, providing valuable insight for debris-flow monitoring. Limitations exist - namely the sensitivity of the estimates of discharge to changes to the channel bed and uncertainties regarding PIV performance. Even though peak discharge may be overestimated in several cases, the scanners' wide spatial distribution and high temporal resolution provide a distinct advantage over systems relying on geophones and radar or ultrasonic gauges, leading to improved and more detailed discharge estimates. As such, the system has been found to provide significant added value to research efforts, but can also be regarded as useful in operational monitoring and warning systems.

Insights gained from a simple indoor experiment supports the chosen approach using PIV, but also highlighted the need to further investigate the key controls on algorithm performance. Additionally, a larger scale approach in a more controlled environment should be considered indispensable to future experiments.

Furthermore, the laser profiles provide unprecedented possibilities for describing and quantifying the lateral surface geometry of debris flows, which are assumed to describe the transition from the coarse-grained head to the watery tail. The selected approach is crude, and may not have been successful in all cases, but the results are nevertheless regarded as significant in promoting further understanding of debris-flow dynamics.

The potential of this dataset has by no means been exhausted by this study. For example, although code has been provided to extract the reflectance data from the raw data files, the potential of these observations has not been explored at all. Furthermore, the profiles are believed to hold unexplored potential for investigating levée building, channel alterations, and flow path variation. Arattano & Marchi (2000) have begun to explore the observed trajectories of boulders in debris-flow fronts, and the displacements computed

with the large-scale PIV approach offer further insights into this topic. Furthermore, the distribution of the flow velocities through time and space has not been investigated, and is certainly worthy of future research. Video is available for some of the events at Dorfbach, which would allow further validation of the velocities computed from the laser data. Although shot at oblique angles, 2-D image coordinates can be transformed to 3-D world coordinates (Arattano & Grattoni, 2000), thus allowing for surface velocities to be computed from the video frames (Genevois et al., 2001; Arattano & Marchi, 2000). The laser surface data could potentially even be merged with video data, to produce 4-D datasets, combining the laser distances with the visual information.

Lastly, only a superficial analysis of the actual discharge results has been undertaken, and this newly created dataset can be harnessed in additional ways – say, to investigate the relationship between total and peak discharge (Marchi et al., 2002; Rickenmann, 1999), to test flow velocity equations (Prochaska et al., 2008; Rickenmann, 1999) or to research frequency-magnitude relations in combination with data from debris-flow events from earlier years. Using the present dataset to validate numerical models in the location where the scanners are located would also be a promising direction for further research.

# Bibliography

- Abellán, A., Jaboyedoff, M., Oppikofer, T., Vilaplana, J. M. 2009. Detection of millimetric deformation using a terrestrial laser scanner: experiment and application to a rockfall event. *Natural Hazards and Earth System Science*, 9, 365–372.
- Arattano, M., Grattoni, P. 2000. Using a fixed video camera to measure debris-flow surface velocity. In: Wieczorek, Naeser (eds.), *Debris-flow hazards mitigation: Mechanics, Prediction, and Assessment*, pp. 273 – 281.
- Arattano, M., Marchi, L. 2000. Video-derived velocity distribution along a debris flow surge. *Physics and Chemistry of the Earth, Part B: Hydrology, Oceans and Atmosphere*, 25, 9, 781–784.
- Arattano, M., Marchi, L. 2005. Measurements of debris flow velocity through cross-correlation of instrumentation data. *Natural Hazards and Earth System Science*, 5, 1, 137–142.
- Arattano, M., Marchi, L. 2008. Systems and sensors for debris-flow monitoring and warning. *Sensors*, pp. 2436–2452.
- Aryal, A., Brooks, B. A., Reid, M. E., Bawden, G. W., Pawlak, G. R. 2012. Displacement fields from point cloud data : Application of particle imaging velocimetry to landslide geodesy. *Journal of Geophysical Research*, 117, 1–15.
- Barboux, C., Delaloye, R., Lambiel, C., Strozzi, T., Collet, C. 2013. Surveying the activity of permafrost landforms in the Valais Alps with InSAR. In: Graf, C. (ed.), *Mattertal–ein Tal in Bewegung*, pp. 7–19.
- Berger, C., McArdell, B. W., Fritschi, B., Schlunegger, F. 2010. A novel method for measuring the timing of bed erosion during debris flows and floods. *Water Resources Research*, 46, 2.
- Biber, P., Andreasson, H., Duckett, T., Schilling, A. 2004. 3D Modeling of Indoor Environments by a Mobile Robot with a Laser Scanner and Panoramic Camera. In:

- 2004 IEEE/RSJ International Conference on intelligent robots and systems (IROS), pp. 3430–3453.
- Colhoun, E. A. 1966. The Debris-Flow at Glendalough, Co. Wicklow and the Bog-Flow at Slieve Rushen, Co. Cavan January 1965. *The Irish Naturalists' Journal*, 15, 7, 199–206.
- Costa, J. E. 1984. Physical Geomorphology of Debris Flows. In: *Developements and Applications of Geomorphology*, chapter 9, pp. 268–317. Springer-Verlag Berlin Heidelberg.
- Danson, F. M., Hetherington, D., Morsdorf, F., Koetz, B., Allgöwer, B. 2007. Forest Canopy Gap Fraction From Terrestrial Laser Scanning. *IEEE Geoscience and Remote Sensing Letters*, 4, 1, 157–160.
- Delaloye, R., Morard, S., Barboux, C., Abbet, D., Gruber, V., Riedo, M., Gachet, S. 2013. Rapidly moving rock glaciers in Mattertal. In: Graf, C. (ed.), *Mattertal – ein Tal in Bewegung*, pp. 21–31.
- Dobson, D. W., Todd Holland, K., Calantoni, J. 2014. Fast, large-scale, particle image velocimetry-based estimations of river surface velocity. *Computers & Geosciences*, 70, 35–43.
- Eisbacher, G. H., Clague, J. J. 1984. *Destructive mass movements in high mountains: hazard and management*. Minister of Supply and Services, Ottawa. 230p.
- Früh, C., Zakhor, A. 2001. 3D Model Generation for Cities Using Aerial Photographs and Ground Level Laser Scans. In: *Proceedings of the 2001 IEEE Computer Society Conference on Computer Vision and Pattern Recognition*, volume II, pp. 31–38.
- Fujita, I., Muste, M., Kruger, A. 1998. Large-scale particle image velocimetry for flow analysis in hydraulic engineering applications. *Journal of Hydraulic Research*, 36, 3, 397–414.
- Genevois, R., Galgaro, a., Tecca, P. 2001. Image analysis for debris flow properties estimation. *Physics and Chemistry of the Earth, Part C: Solar, Terrestrial & Planetary Science*, 26, 9, 623–631.
- Gonzalez, R. C., Woods, R. E. 2008. *Digital Image Processing*. Pearson Education International, Upper Saddle River, New Jersey, 07458, 3rd edition.

- Graf, C., McArdell, B. 2005. Die Murgangbeobachtungsstation Randa. Birmensdorf, Eidg. Forschungsanstalt WSL, pp. 1–6.
- Graf, C., Deubelbeiss, Y., Bühler, Y., Meier, L., McArdell, B. W., Christen, M., Bartelt, P. 2013. Gefahrenkartierung Mattertal: Grundlagenbeschaffung und numerische Modellierung von Murgängen. In: Graf, C. (ed.), Mattertal – ein Tal in Bewegung, pp. 85–112.
- Graf, W. L. 1970. The Geomorphology of the Glacial Valley Cross Section. *Arctic and Alpine Research*, 2, 4, 303–312.
- Gruber, S., Haeberli, W. 2009. Mountain permafrost. In: Margesin, R. (ed.), *Permafrost soils*, pp. 33–44. Springer. Bio. Series 16.
- Holland, K., Puleo, J., Kooney, T. 2001. Quantification of swash flows using video-based particle image velocimetry. *Coastal Engineering*, 44, 2, 65–77.
- Hu, H., Saga, T., Kobayashi, T., Okamoto, K., Taniguchi, N. 1998. Evaluation of the Cross Correlation Method by Using PIV Standard Images. *Journal of Visualization*, 1, 1, 87–94.
- Huggel, C., Clague, J. J., Korup, O. 2012. Is climate change responsible for changing landslide activity in high mountains? *Earth Surface Processes and Landforms*, 37, 1, 77–91.
- Hungr, O. 2000. Analysis of debris flow surges using the theory of uniformly progressive flow. *Earth Surf. Process. Landforms*, 25, 483 – 495.
- Hungr, O., Evans, S. G., Bovis, M. J., Hutchinson, J. N. 2001. A Review of Classification of Landslides of the Flow Type. *Environmental & Engineering Geoscience*, 7, 3, 221–238.
- Hungr, O., McDougall, S., Bovis, M. J. 2008. Entrainment of material by debris flows. In: Jakob, M., Hungr, O. (eds.), *Debris-flow Hazards and Related Phenomena*, p. 795. Springer.
- Hürlimann, M., Rickenbach, D., Graf, C. 2003. Field and monitoring data of debris-flow events in the Swiss Alps. *Can. Geotech. J.*, 40, 161 – 175.
- Hürlimann, M., Rickenmann, D., Medina, V., Bateman, A. 2008. Evaluation of approaches to calculate debris-flow parameters for hazard assessment. *Engineering Geology*, 102, 3-4, 152–163.

- Im, J., Jensen, J. R., Tullis, J. A. 2008. Object-based change detection using correlation image analysis and image segmentation. *International Journal of Remote Sensing*, 29, 2, 399–423.
- Itakura, Y., Inaba, H., Sawada, T. 2005. A debris-flow monitoring devices and methods bibliography. *Natural Hazards and Earth System Science*, 5, 971–977.
- Iverson, R. 1997. The physics of debris flows. *Reviews of geophysics*, 35, 3, 245–296.
- Iverson, R. 2003. The debris-flow rheology myth. In: Rickenmann, D., Chen, C.-I. (eds.), *Debris-flow hazards mitigation: mechanics, prediction and assessment*, pp. 303–314.
- Iverson, R. M., Logan, M., LaHusen, R. G., Berti, M. 2010. The perfect debris flow? Aggregated results from 28 large-scale experiments. *Journal of Geophysical Research*, 115, F3, F03005.
- Jacquemart, M., Tobler, D., Graf, C., Meier, L. 2015. Advanced Debris-Flow Monitoring and Warning System at Spreitgraben. In: Lollino, G., Arattano, M., Rinaldi, M., Giustolisi, O., Marechal, J.-C., Grand, G. E. (eds.), *Engineering Geology for Society and Territory*, volume 3, pp. 59–62.
- Kenner, R., Bühler, Y., Delaloye, R., Ginzler, C., Phillips, M. 2014. Monitoring of high alpine mass movements combining laser scanning with digital airborne photogrammetry. *Geomorphology*, 206, 492–504.
- Kober, F., Hippe, K., Salcher, B., Ivy-Ochs, S., Kubik, P. W., Wacker, L., Hählen, N. 2012. Debris-flow-dependent variation of cosmogenically derived catchment-wide denudation rates. *Geology*, 40, 10, 935–938.
- Le Coz, J., Hauet, a., Pierrefeu, G., Dramais, G., Camenen, B. 2010. Performance of image-based velocimetry (LSPIV) applied to flash-flood discharge measurements in Mediterranean rivers. *Journal of Hydrology*, 394, 1-2, 42–52.
- Leese, J. A., Novak, C., Clark, B. 1971. An Automated Technique for Obtaining Cloud Motion from Geosynchronous Satellite Data using Cross Correlation. *J. of Appl. Meteorol.*, 10, 118–132.
- Li, D., Zhong, Q., Yu, M., Wang, X. 2013. Large-scale particle tracking velocimetry with multi-channel CCD cameras. *International Journal of Sediment Research*, 28, 1, 103–110.

- Li, Y., Liu, G., Cui, Z. 2001. Glacial valley cross-profile morphology, Tian Shan Mountains, . *Geomorphology*, 38, 153–166.
- Lindeberg, T. 1998. Feature detection with automatic scale selection. *International journal of computer vision*, 30, 2, 79–116.
- Lloyd, M. P., Ball, D. J., Stansby, P. K. 1995. Unsteady Surface-Velocity Field Measurements Using Particle Tracking Velocimetry. *J. of Hydraulic Research*, 33, 4, 519–534.
- Marchi, L., D’Agostino, V. 2004. Estimation of debris-flow magnitude in the Eastern Italian Alps. *Earth Surface Processes and Landforms*, 29, 2, 207–220.
- Marchi, L., Arattano, M., Deganutti, A. M. 2002. Ten years of debris-flow monitoring in the Moscardo Torrent (Italian Alps). *Geomorphology*, 46, 1-2, 1–17.
- Mathworks. 2012. Matlab release 2012b. The Mathworks, Inc, Natick, Massachusetts, United States.
- Mazzarini, F., Pareschi, M. T., Favalli, M., Isola, I., Tarquini, S., Boschi, E. 2007. Lava flow identification and aging by means of lidar intensity: Mount Etna case. *Journal of Geophysical Research*, 112, B2, B02201.
- McArdell, B. W., Bartelt, P., Kowalski, J. 2007. Field observations of basal forces and fluid pore pressure in a debris flow. *Geophysical Research Letters*, 34, 7, L07406.
- McCoy, S. W., Kean, J. W., Coe, J. a., Staley, D. M., Wasklewicz, T. a., Tucker, G. E. 2010. Evolution of a natural debris flow: In situ measurements of flow dynamics, video imagery, and terrestrial laser scanning. *Geology*, 38, 8, 735–738.
- Mendes, A., Bento, L., Nunes, U. 2004. Multi-target detection and tracking with a laserscanner. *IEEE Intelligent Vehicles Symposium*, 2004, pp. 796–801.
- Meunier, P., Leweke, T. 2003. Analysis and treatment of errors due to high velocity gradients in particle image velocimetry. *Experiments in Fluids*, 35, 5, 408–421.
- Muste, M., Fujita, I., Hauet, A. 2008. Large-scale particle image velocimetry for measurements in riverine environments. *Water Resources Research*, 44, 4.
- Osaka, T., Takahashi, E., Kunitomi, M., Yamakoshi, T., Nowa, Y., Kisa, H., Ishizuka, T., Utsunomiya, R., Yokoyama, K., Mizuyama, T. 2013. Field observations of unit weight of flowing debris flows by force plate in Sakurajima, Japan. *Journal of the Japan Society of Erosion Control Engineering*, 65, 6, 46–50.

- Pan, B., Qian, K., Xie, H., Asundi, A. 2009. Two-dimensional digital image correlation for in-plane displacement and strain measurement: a review. *Measurement Science and Technology*, 20, 6, 1–17.
- Pattyn, F., van Huele, W. 1998. Power law or power law? *Earth Surface Processes and Landforms*, 23, 761–767.
- Pierson, T. C. 1986. Flow behavior of channelized debris flows, Mount St. Helens, Washington. In: Abrahams, A. D. (ed.), *Hillslope Processes*, pp. 269 – 296. Allen and Unwin, Boston.
- Prochaska, A. B., Santi, P. M., Higgins, J. D., Cannon, S. H. 2008. A study of methods to estimate debris flow velocity. *Landslides*, 5, 4, 431–444.
- Pudasaini, S. P., Wang, Y., Hutter, K. 2005. Modelling debris flows down general channels. *Natural Hazards and Earth System Science*, 5, 6, 799–819.
- Raffel, M., Willert, C. E., Wereley, S. T., Kompenhans, J. 2007. *Particle Image Velocimetry, A Practical Guide*. Oxford Univ. Press, New York.
- Rickenmann, D. 1999. Empirical relationships for debris flows. *Natural hazards*, 19, 1, 47–77.
- Rickenmann, D., Laigle, D., McArdell, B. W., Hübl, J. 2006. Comparison of 2D debris-flow simulation models with field events. *Computational Geosciences*, 10, 2, 241–264.
- Scambos, T. A., Dutkiewicz, M. J., Wilson, J. C., Bindenschadler, R. A. 1992. Application of image cross-correlation to the measurement of glacier velocity using satellite image data. *Remote Sensing of Environment*, 42, 3, 177–186.
- Schneider, F. D., Leiterer, R., Morsdorf, F., Gastellu-Etcheberry, J.-P., Lauret, N., Pfeifer, N., Schaepman, M. E. 2014. Simulating imaging spectrometer data: 3D forest modeling based on LiDAR and in situ data. *Remote Sensing of Environment*, 152, 235–250.
- Schubert, A., Faes, A., Käab, A., Meier, E. 2013. Glacier surface velocity estimation using repeat TerraSAR-X images: Wavelet- vs. correlation-based image matching. *ISPRS Journal of Photogrammetry and Remote Sensing*, 82, 49–62.
- Schürch, P., Densmore, a. L., Rosser, N. J., McArdell, B. W. 2011. Dynamic controls on erosion and deposition on debris-flow fans. *Geology*, 39, 9, 827–830.



- Shan, J., Toth, C. K. (eds.). 2009. Topographic Laser Ranging and Scanning: Principles and Processing. CRC Press Taylor and Francis Group.
- SICK. 2010. Lasermesssensoren der Produktfamilie LMS5xx - Betriebsanleitung. Technical report, SICK AG Waldkirch, Reute, Germany.
- Stahn, R., Stopp, A. 2007. Ein Lasersensor-basiertes Navigationssystem für Nutzfahrzeuge. In: Berns, K., Luksch, T. (eds.), *Autonome Mobile Systeme*, pp. 184–190. Springer Berlin Heidelberg.
- Staley, D. M., Wasklewicz, T. A., Coe, J. A., Kean, J. W., Mccoy, S. W., Tucker, G. E. 2011. Observations of debris flows at Chalk Cliffs, Colorado, USA : Part 2, changes in surface morphometry from terrestrial laser scanning in the summer of 2009.
- Stanislas, M., Okamoto, K., Kähler, C. J., Westerweel, J., Scarano, F. 2008. Main results of the third international PIV Challenge. *Experiments in Fluids*, 45, 1, 27–71.
- Stevens, C., Coates, M. 1994. Applications of a maximized cross-correlation technique for resolving velocity-fields in laboratory experiments. *Journal of Hydraulic Research*, 32, 2, 195–212.
- Svensson, H. 1958. Is the cross-section of a glacial valley a parabola? *Journal of Glaciology*, 3, 362–363.
- Theunissen, R., F, S., L, R. M. 2007. An adaptive sampling and windowing interrogation method in PIV. *Measurement Science and Technology*, 18, 1, 275 – 287.
- Theunissen, R., F, S., L, R. M. 2010. Spatially adaptive PIV interrogation based on data ensemble. *Experiments in Fluids*, 84, 875–887.
- Tobler, D., Kull, I., Hählen, N. 2012. Gefahrenmanagement der Murgänge im Spreitgraben, Guttannen. *Swiss Bulletin for Applied Geology*, 17, 2, 53–61.
- Tobler, D., Kull, I., Jacquemart, M., Haehlen, N. 2014. Hazard Management in a Debris Flow Affected Area: Case Study from Spreitgraben, Switzerland. In: Sassa, K., Canuti, P., Yin, Y. (eds.), *Landslide Science for a Safer Geoenvironment*, volume 3, pp. 25–30. Springer International Publishing.
- Toyos, G., Gunasekera, R. 2008. GIS-assisted modelling for debris flow hazard assessment based on the events of May 1998 in the area of Sarno, Southern Italy: II. Velocity and dynamic pressure. *Earth Surface Processes and Landforms*, 1708, 1693–1708.

- Travelletti, J., Malet, J.-P., Delacourt, C. 2014. Image-based correlation of Laser Scanning point cloud time series for landslide monitoring. *International Journal of Applied Earth Observation and Geoinformation*, 32, 1–18.
- Vosselman, G., Maas, H.-G. (eds.). 2010. *Airborne and Terrestrial Laser Scanning*. Whittles Publishing.
- Ye, C., Borenstein, J. 2002. Characterization of a 2D laser scanner for mobile robot obstacle negotiation. In: *Proceedings 2002 IEEE International Conference on Robotics and Automation* (Cat. No.02CH37292), volume 3, pp. 2512–2518.
- Yoneda, K., Tehrani, H., Ogawa, T., Hukuyama, N., Mita, S. 2014. Lidar Scan Feature for Localization with Highly Precise 3-D Map. In: *2014 IEEE Intelligent Vehicles Symposium*, Iv, pp. 1345–1350.
- Zhang, Z., Wang, X., Fan, T., Xu, L. 2013. River surface target enhancement and background suppression for unseeded LSPIV. *Flow Measurement and Instrumentation*, 30, 99–111.

# A Technical summaries

## A.1 SICK LMS 511 laser scanner

	Randa setup	Spreitgraben setup
Operating wavelength	IR (905 nm)	IR (905 nm)
Opening angle	190°	190°
Scan frequency	25 Hz – 100 Hz	25 Hz – 100 Hz
Angular resolution	0.167° – 1°	0.167° – 1°
Distance range (@ 10% object reflectivity)	0.7 m – 26m	1 m – 40m
Maximum range	65 m	65 m
Heating	yes	yes
Beam divergence	11.9 mrad	3.6 mrad
Number of responses	5	5
Systematic error (@ 10% object reflectivity)	1 m - 10 m: ± 25 mm	1 m - 10 m: ± 25 mm
	10 m - 20 m: ± 35 mm	0 m - 20 m: ± 35 mm
	20 m - 30 m: ± 50 mm	n.a.
Random error (@ 10% object reflectivity)	1 m - 10 m: ± 6 mm	1 m - 10 m: ± 7 mm
	10 m - 20 m: ± 8 mm	0 m - 20 m: ± 9 mm
	20 m - 30 m: ± 14 mm	n.a.
Weight:	3.7 kg	3.7 kg
Dimension	160 mm x 155 mm x 185 mm	160 mm x 155 mm x 185 mm

Table A.1: Summary of essential technical characteristics of the SICK LMS 511 profile scanner.

## B Flow depths results

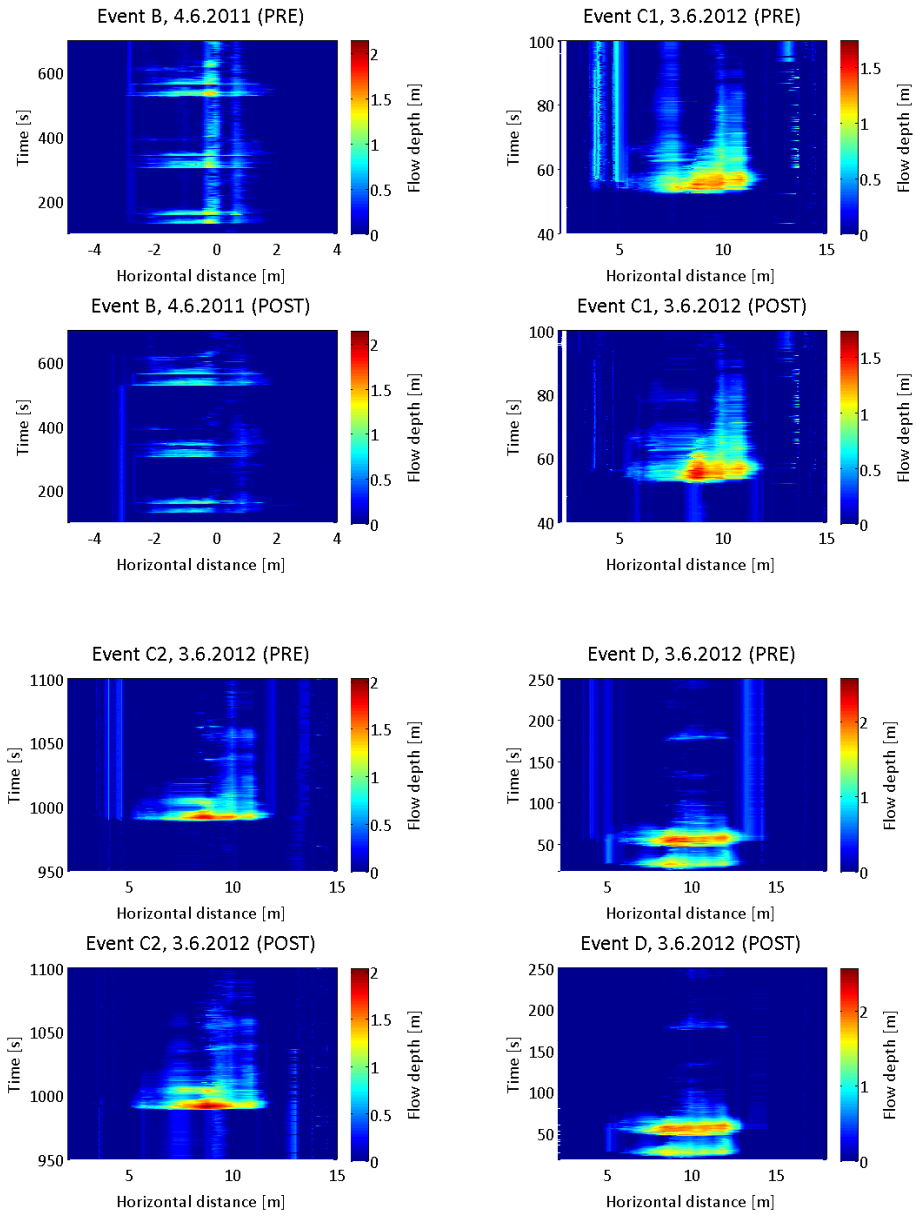


Figure B.1: Flow depth results B–D

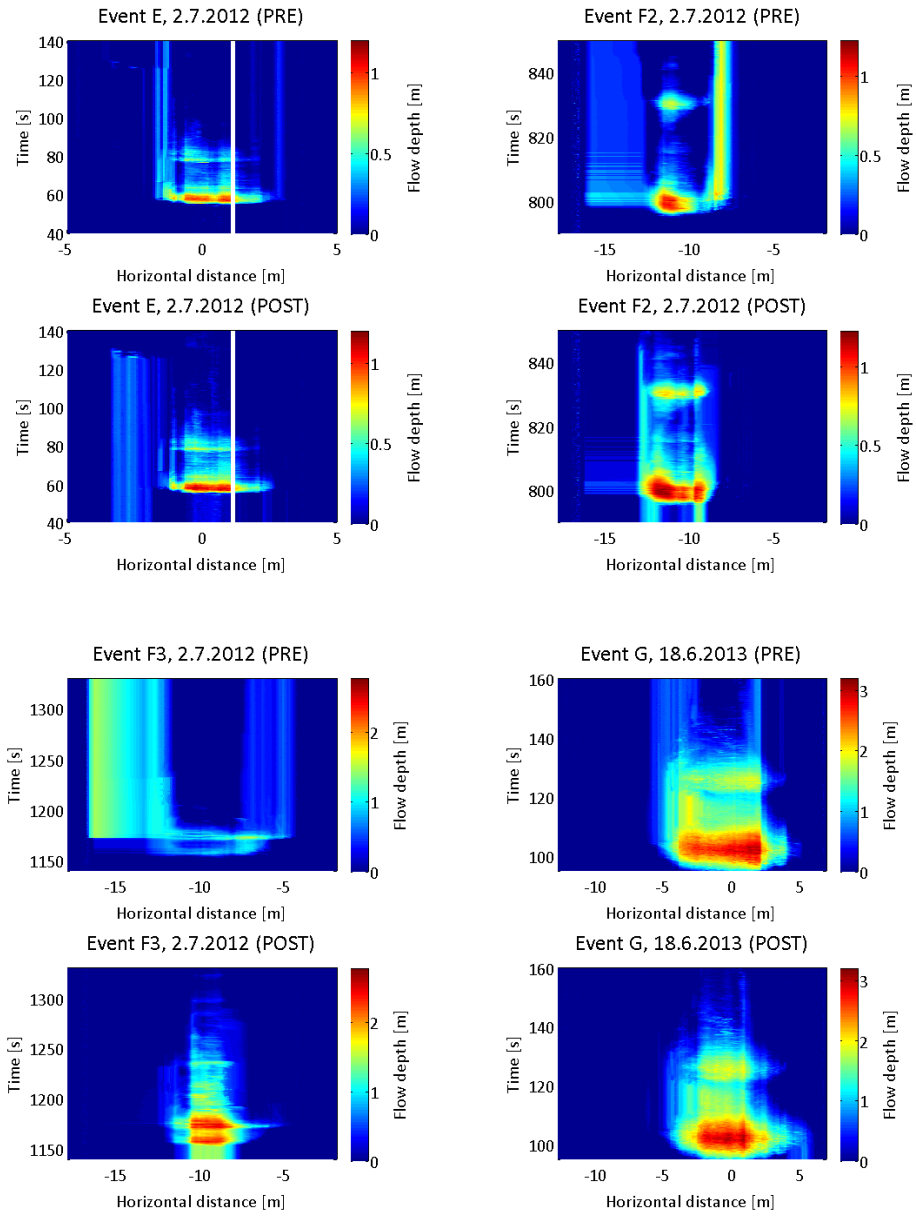


Figure B.2: Flow depth results E–G

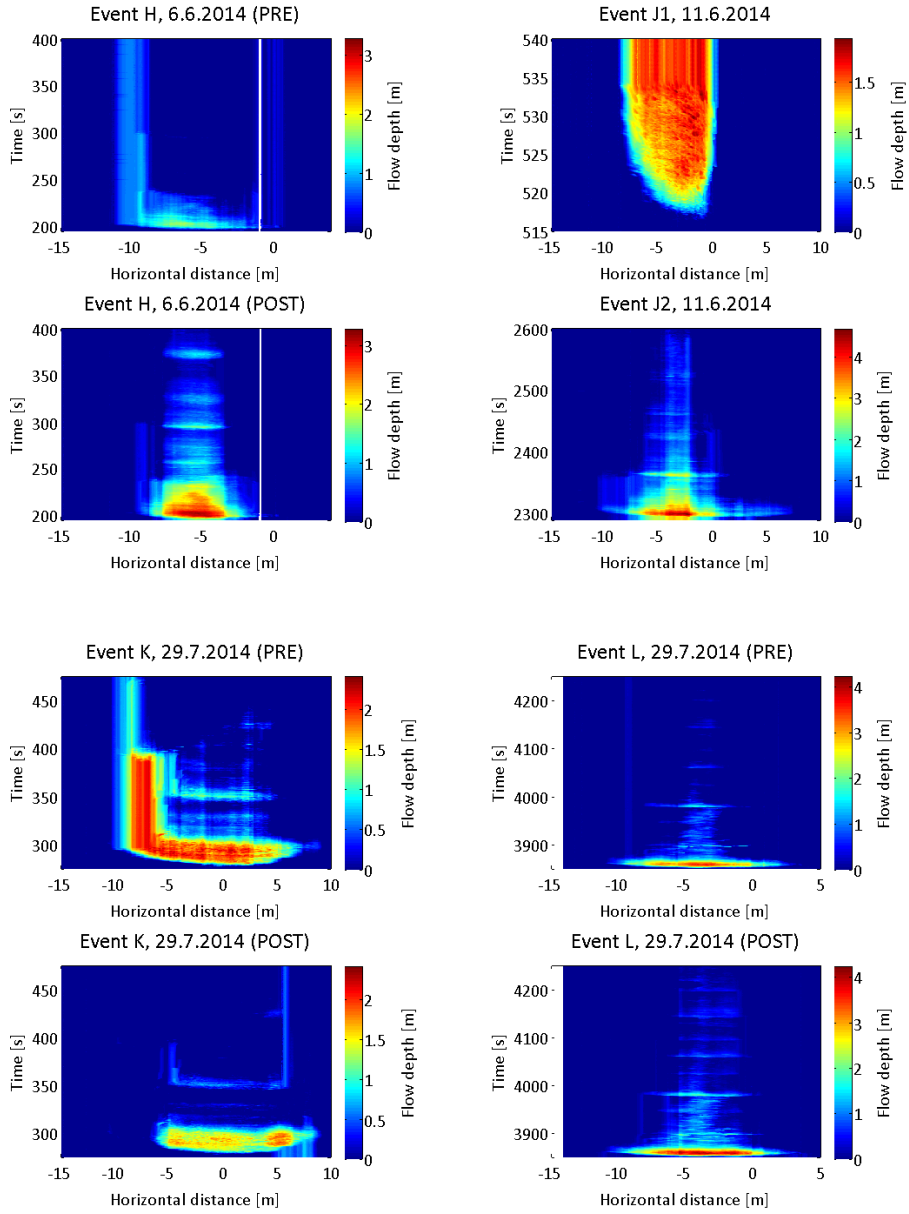


Figure B.3: Flow depth results H–L

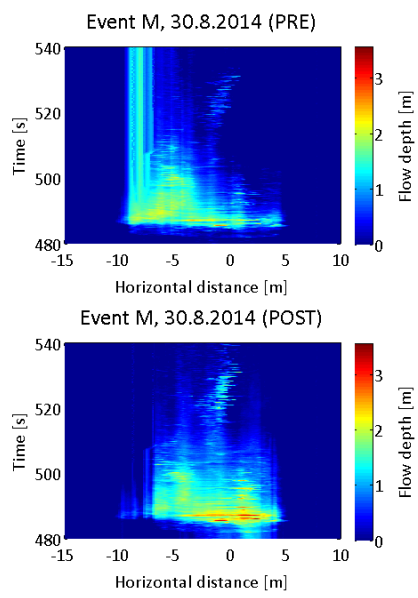


Figure B.4: Flow depth results M



## C Flow velocity results

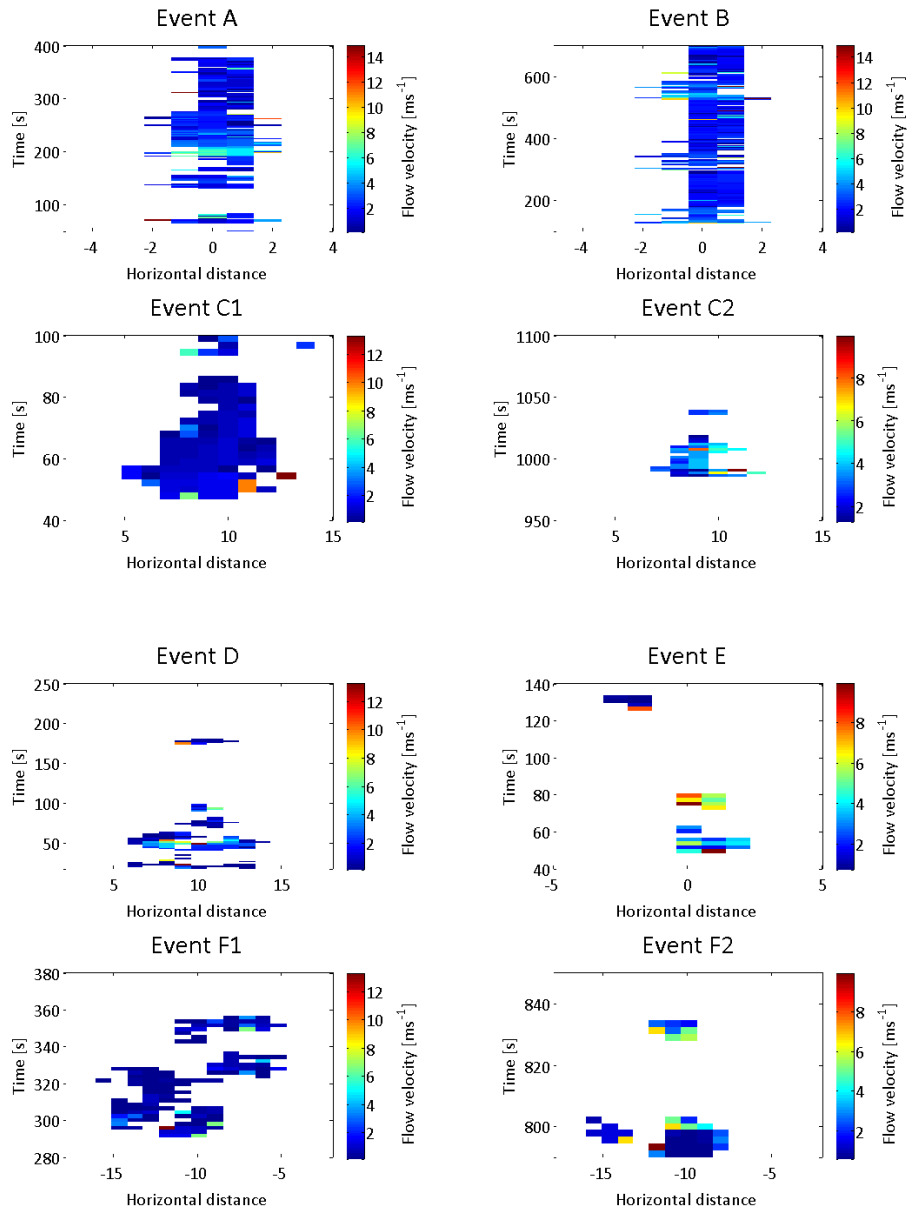


Figure C.1: Flow depth results A – F2

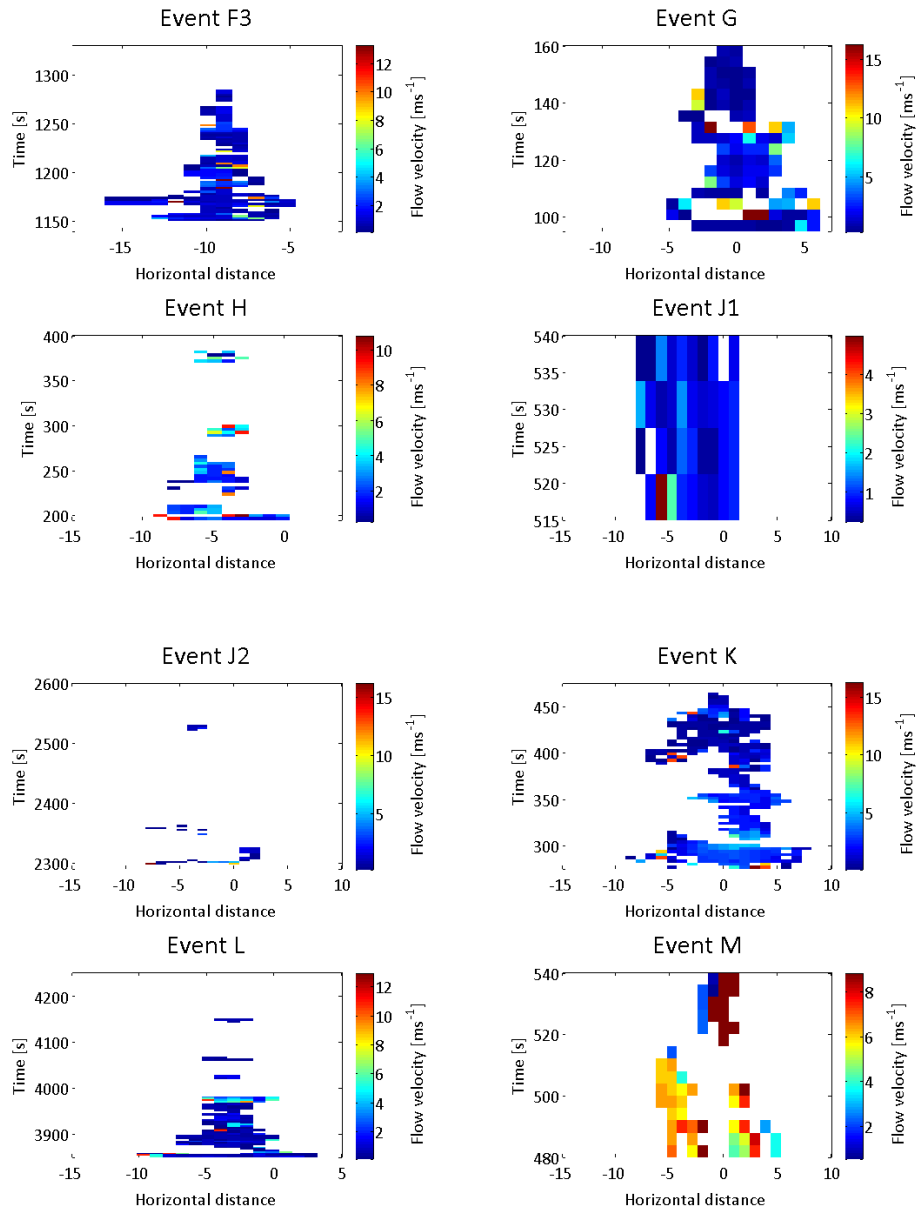


Figure C.2: Flow depth results F3–M

## D Experiment flow velocities

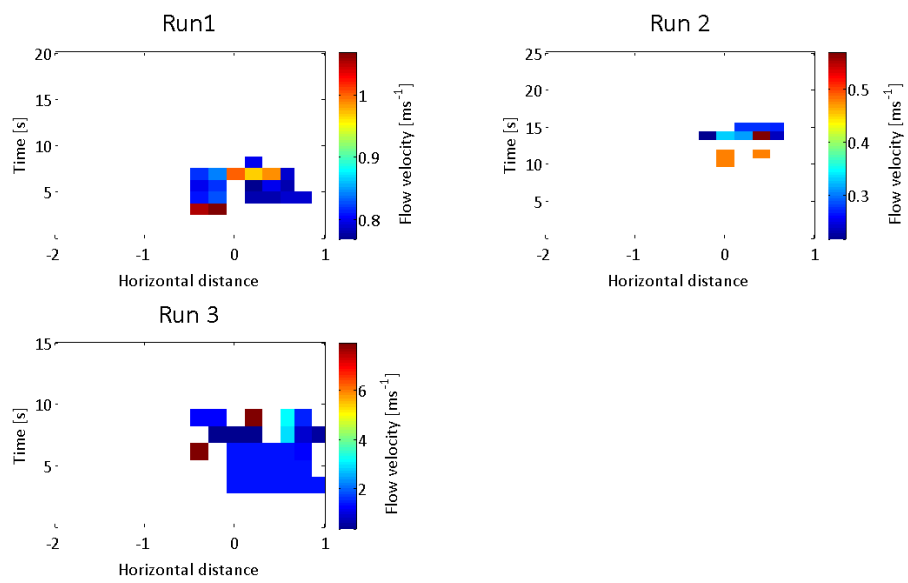


Figure D.1: Flow velocities from indoor experiment

# E Technical documentation

The following documentation is intended for anyone interested in using the provided code to compute flow height, flow velocity and discharge values from SICK profile scanner datasets of debris flows, and the described variables refer to the ones implemented in the code (digitally available on the CD handed in with the thesis or from the autor). In some cases, they may differ slightly from descriptions in the Methods chapter. Additional help is also provided by the comments found in the code itself. For background on the implemented LSPIV approach, the reader is referred to the description of Methods in Chapter 2.

## E.1 A: Raw data processing

Script A contains all the tools to read the raw data, and perform basic data- and noise reduction steps. Both distance and reflectance matrices can be computed.

### 1 Define basic parameters

For reading the raw data, only the serial numbers of the scanners need to be known and defined, as well as the directory where the raw data files are stored. The scanner serial number is necessary in order to separate scan lines from the two scanners as these are written into the same raw data file. Scanner number 1 is defined as the upriver scanner whereas scanner number 2 is defined as the downriver scanner.

### 2 Read data

Once the inputs variables needed to read the raw data are defined, four variables are extracted from the raw data, using the function `ReadLMSFilesOld`. The variable *angle* contains a vector of  $0.5^\circ$  (or  $0.3333^\circ$ ) intervals centered around  $90^\circ$  (nadir). The *dist* variable contains the distance measurements for every angle interval, while the *refl* variable contains the corresponding RSSI values. Lastly, the *scan* variable holds the metadata for every registered line for both scanners, notably computer time, scanner serial, scanner errors, scanner time etc. Finally, the scan lines from the lower scanner need to be reversed (mirrored across the center of the x-axis)

because it is mounted in the opposite way. In order to be able to reload the results from this processing step at any time, the four variables *angle*, *dist*, *refl* and *scan* as well as the scanner serial numbers and the indexes relating the measurements to the two scanners are saved to file.

### 3 Define across-bed extent

In order to be able to interpolate the irregularly spaced data points from the raw data onto a regular grid, a symmetrical across-bed x-axis needs to be defined by the user. To facilitate this, the raw data is visualized in a simple plot for the user to decide on the maximum extent needed and to verify the data content. A color plot generated at the end lets the user evaluate the data content.

### 4 Construct distance matrix

The raw data consists of subsequent measurements of distance and angle in a polar coordinate system. As illustrated in Figure E.1 on page 76 these coordinates can easily be transformed into a cartesian coordinate system by computing, for every point on every scan line along t:

$$x_t = \rho_t * \cos(\theta_t)$$

$$y_t = \rho_t * \sin(\theta_t)$$

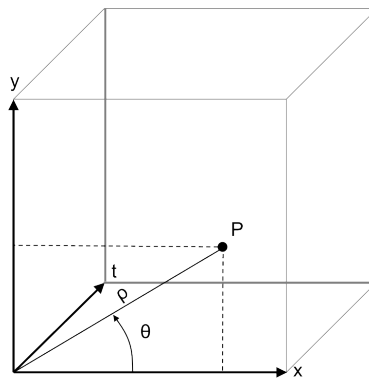


Figure E.1: The polar coordinates describing the raw data as angle ( $\theta$ ) and distance from the laser ( $\rho$ ) are transformed into cartesian x and y values for every raw data point P along every scan line along t.

Now the points are unevenly spaced across the x-axis, while they are evenly spaced along the time axis t. In order to facilitate further processing, the data are inter-

polated onto an evenly spaced grid with a grid size of 50mm per default (variable *samplingx*, making up the x-axis (*xax*)). The resulting matrix *yxt* takes the form of:

$$yxt_{t_x} = \begin{pmatrix} y_{11} & y_{12} & \cdots & y_{1x} \\ y_{21} & y_{22} & \cdots & y_{2x} \\ \vdots & \vdots & \ddots & \vdots \\ y_{t1} & y_{t2} & \cdots & y_{tx} \end{pmatrix}$$

Again, in order to be able to continue from this point at any time, the defined x-axis variables *xax* and *samplingx* are stored to file alongside the distance matrix.

## 5 Crop Matrix

The interpolation onto an evenly spaced grid works on a symmetric x-axis. In many cases however, the necessary extent of the x-axis is not equal on both sides of the debris-flow channel, hence an x-axis with a larger extent than necessary is defined initially. Mostly, the raw data also comprises more data than is of interest in the time direction. The size of the *yxt* matrix resulting from the coordinate transformation and interpolation can thus be reduced. Four inputs are required to crop the matrix to the necessary extent. All four can be easily read from the graph that is automatically computed: In the x-direction, the left and right hand extremes need to be defined, while a starting point and an end point along the time axis are also required. The cropped matrix is saved to file, again together with the corresponding x-axis variables that allow the user to continue working with this matrix only, without having to remember the defined x-axis settings.

## 6 Construct intensity variable

The reflectance value drawn from the raw data is an RSSI (Received Signal Strength Indicator) value scaled between 0 and 255. This value is normalized such that:

$$I_{\text{norm}} = \text{RSSI} \cdot \left(\frac{d}{n}\right)^2$$

where: RSSI=signal strength value; d=slant range distance; n=normalization distance.

## 7 Averaging lines

In order to reduce the amount of data, one possibility is to average several lines, thus reducing the sampling rate. This represents a 'block-average' approach, where

a defined number of consecutive lines are averaged along the y-axis, while retaining the full resolution along x. The number of averaged lines needs to be an integer coefficient of the sampling rate. The results of this processing are saved to a file that also contains the number of averaged lines as a variable.

## **8 Median filter**

A certain amount of salt-and-pepper noise is expected from splashing, rain or water dripping from the scanner platform. A simple approach to reduce this type of noise is to use a median filter. In order to retain the maximum amount of surface information, the residuals between the filtered surface and the original data are computed, and only the points exceeding three standard deviations of the residuals are deleted. The user is asked to define the window size used in the filtering. The resulting matrix is saved to a new file again.

## **E.2 B: Debris flow analysis**

Script B contains all the necessary processing steps to isolate events of interest and to compute flow depth, flow velocities and discharge values for these.

### **1 Load matrix and define basic parameters**

Once the matrix that needs to be processed is loaded, a few additional parameters need to be defined, namely the the number of lines averaged in the file and the choice of whether the up or the downstream scanner shall be used for the computation of the bed geometry. The effective sampling rate is automatically computed from the original sampling rate and the number of averaged lines. The user is also asked to give event date and location. This is used to generate correct plot titles. The distance between the two scanners (variable *dScanners*) is also set per default, but might have to be adjusted in case of differing setups.

### **2 Isolate event**

An isolation of single surges or events is possible by defining the lower and upper time index in seconds. In order to facilitate this, an overview plot showing an across-bed view as well as a time-axis view is generated. The user can easily define the boundaries of the event of interest in seconds. The start-time needs to be at least 11 seconds, because the ten seconds prior to the event are evaluated for the bed geometry. In some instances it might be desirable to use a post-bed geometry rather than a pre-event one. A small block of code can be uncommented to achieve this by simply using ten seconds of data after the event to compute the bed geometry.



### 3 Bed geometry and flow depth

The assumed bed geometry needed to compute flow depth is calculated, for every position along  $x$ , as:

$$\text{bedgeom}_x = \frac{1}{T} \sum_{t=1}^N y_x(t)$$

where  $T$  is the length of the pre or post-event time index *tidx1*, and  $y$  and  $x$  are positions on the cartesian coordinate system.

With a known bed profile, the flow height can be computed for every scan line following

$$\text{FlowHeight}_{xt} = \begin{cases} 0, & \text{if } y_{xt} \leq \text{bedgeom}_x \\ y_{xt} - \text{bedgeom}_x, & \text{if } y_{xt} > \text{bedgeom}_x \end{cases}$$

The bed geometry and flow height are computed from the data of one scanner (as defined in *scnr*) only.

### 4 Parameters for velocity computation

For the subsequent velocity computation several parameters need to be defined by the user, others are set per default, but can of course be altered. An overview is given in Table E.1 on page 79. Further details are also given in the description of the algorithm below.

Variable name	Description	Unit	User interaction
vmax	Maximum expected flow velocity	m/s	u
vmin	Minimum expected flow velocity	m/s	u
mincorrneeded	Correlation threshold	-	d
reslateral	Desired across-bed size of the interrogation area	mm	u
xcorrwin	Number of cells corresponding to <i>reslateral</i>	-	a
lowscidx	Temporal range that needs to be considered for correlation	s	a
corrwin	Length of correlation window in the temporal dimension	-	a
stepsize	Time-index steps between two correlation runs	-	d

Table E.1: List of all parameters required for the computation of the flow velocities. User interaction 'u' denotes parameters that can be defined by the user, 'd' denotes parameters that are set per default or computed automatically ('a').

### 5 Velocity computation

The basic code for the velocity computation was received from Dr. Lorenz Meier

and has been altered and expanded. The basic concept behind the velocity computation using the LSPIV approach is a 2-D correlation analysis for which Matlab offers the function *xcorr2*. The 2-D cross-correlation of an M-by-N matrix X and an P-by-Q matrix H is a matrix C of the size M+P-1 by N+Q-1, computed as:

$$C(k,l) = \sum_{m=0}^{M-1} \sum_{n=0}^{N-1} X(m,n) \overline{H}(m-k, n-l),$$

$$-(P-1) \leq k \leq M-1,$$

$$-(Q-1) \leq l \leq N-1$$

where  $\overline{H}$  denotes the complex conjugation. The cross-correlation is not computed for the entire matrix, but for spatio-temporal subsets of it, in order to find the offset in time between each matrix subset of the first scanner and the corresponding subset from the second scanner. The following list briefly describes how the matrix subsets are computed and processed to derive flow velocities.

1. The temporal subdivision depends on the expected flow velocities. For very slow processes, the time-window that needs to be searched for high correlation needs to be longer than for fast movements. On the other hand, if the expected velocity is high, the delay to the onset of the search-window from the lower scanner has to be minimal. Thus the temporal extent for the sub-matrices is defined through the expected maximum and minimum velocities *vmax* and *vmin*. In the time direction, a new 2-D cross-correlation is computed in steps of a fourth of the length of the correlation window. Doing this, every shift of the correlation-window in time sets a step-counter *tnr* up by one.
2. The spatial subdivision also needs to be defined. This *reslateral* parameter should be constrained by the expected size of objects, a value that can potentially be guessed from event imagery. It defines the width of the interrogation area (IA) where

$$xcorrwin = \text{round} \left( \frac{\textit{lateral resolution}}{\textit{pixel size}} \right)$$

3. High-pass filtering: In a further step, the single subsets are filtered to retain only the surface roughness information. Up to this point, matrix y-values are in the order of several meters (distance from the scanner in the cartesian co-

ordinate system). A simple high-pass filtering is performed by approximating a second order polynomial of the form

$$pp(t) = at^2 + bt + c$$

to each column along x and then retaining only the differences

$$scfilt = y(t) - pp(t)$$

for further analysis.

4. Now the spatial (lateral, along x) subdivision is performed by use of *xcorrwin*. These subsets are referred to as *sc1fpart* and *sc2fpart*, where *sc1fpart* is the IA and *sc2fpart* is the search area (SA). SA is defined to be three times as wide as IA. Again, for every loop performed in the across-bed direction, a step-counter *xnr* is increased by one.
5. Hence, one spatio-temporal subset from each scanner goes into the 2-D cross correlation, and the correlation matrix is computed from this data. At the same time, the maximally possible cross-correlation is computed for every correlation area as:

$$NN = \sqrt{\sum_{i=1}^m \sum_{j=1}^n sc1filt_{ij} sc1filt_{ij} \cdot \sum_{i=1}^m \sum_{j=1}^n sc2filt_{ij} sc2filt_{ij}}$$

All values  $NN_{tnr,xnr}$  are retained for further normalization of the  $C_{tnr,xnr}$  matrix in

$$C_{norm} = \left( \frac{C_{tnr,xnr}}{\max(NN)} \right)$$

6. The variable *Quality* represents the size (number of cells) of the cross-correlation maximum, calling for a minimum of 18 cells to attain a value of 0.7 of the maximum itself. If the quality is lower, the corresponding cross-correlation cell is disregarded.
7. Finally, the index of the cell containing the maximum correlation from within the correlation-matrix is computed in order to obtain the shift in time and space. In the temporal dimension, only cells with negative lags are used, i.e. cells where the upper scanner is first. In the spatial dimension the index is needs to be corrected by the size of the matrix subset along x. The flow

velocity for each correlation window can then be computed as:

$$\vec{v}_{\text{tnr,xnr}} = \left( \frac{T_{\text{tnr,xnr}}}{d\text{Scanners}} \right) \quad (\text{E.1})$$

Where  $\vec{v}$  is the flow velocity for the cell (tnr,xnr), T is the time lag in seconds and  $d\text{Scanners}$  is the distance between the scanners in meters. In order to be retained, a cells'  $C_{\text{norm}}$  and  $Quality$  values must exceed the defined thresholds of 0.1 and 18, respectively.

## 7 Hydrograph Computation

The flow depth (equation 2.3) and the cell velocities (equation E.1) are subsequently used to compute discharge. Flow depth and flow velocities need to be rescaled to matching resolutions. This is achieved by resampling the flow velocity matrix to the resolution of the flow height matrix using a nearest neighbor resampling technique (matrix *ResizeFlowVelocity*). Where the quality requirements are not met, no velocity estimates are available. This circumstance is partly counteracted by extrapolating the flow velocity values in relation to flow depth. An extrapolation is only performed along the single scan lines. For lines without any velocity information, no extrapolation is performed. The extrapolated flow velocities are calculated as:

$$\overrightarrow{\text{ExtrapVel}}_{t,x} = \tilde{v}_t \cdot \frac{h_{t,x}}{\max(h_t)}$$

For every row in time,  $Q_{\text{line}}$  can then be computed as:

$$Q_{\text{line}} = \sum_{x=1}^X \text{FlowDepth}_{t,x} \cdot \frac{\text{sampling}_x}{1000} \cdot \vec{v}_{t,x}$$

and to obtain total discharge  $Q_{\text{tot}}$

$$Q_{\text{tot}} = \frac{1}{r} \sum_{t=1}^N Q_{\text{line}}(t)$$

where  $r$  is the sampling rate.

Alongside the hydrograph computation, several plots are generated, showing the velocity extrapolation, flow height vs. flow depth, as well as the final hydrograph plot. In the hydrograph, black line sections denote that the discharge was computed

using the overall mean velocity.

### **8 Save data to OUTPUT-structure**

To facilitate later evaluation of the processed data, all significant values and variables are saved into a Matlab-structure. Table E.2 on page 84 describes the stored variables.

### **9 Data animation**

This block of code generates an animation of the profile lines contained within the defined time index in an .AVI file. The axis needs to be adjusted to comprise the wanted extent, and the location of the text showing time also.

Field name	Description
<b>Outputs</b>	
Date	Specified event date
AveragedLines	Number of lines that were averaged
Samplingrate	Samplingrate computed from original scan rate and number of averaged lines.
TIndx	Time index evaluated
BedIndx	Time index used for bed geometry computation
Bedgeometry	Vector containing the computed bed geometry
Discharge	Discharge vector
Qtot	Total discharge
Qmax	Peak discharge
Vmax	Maximum velocity
Vmean	Average velocity
Vmed	Median velocity
FlowVel	Flow velocities matrix
FlowDepth	Flow depth matrix
Hmax	Maximum flow depth
CorrQuality	Matrix of correlation quality values
CorrCount	Number of cells that yielded a correlation above the specified correlation threshold.
MinCorrNeeded	Specified correlation threshold.
Comments	Field for various comments.
<b>General settings</b>	
time	Time vector specified to isolate event, temporal axis
samplingx	spatial resolution in across bed direction (matrix interpolation steps)
scnr	Scanner number; Defines the scanner that is used to compute the bed geometry.
xax	matrix x-axis (across bed axis)
vmin, vmax, res-lateral, lowscidx, corrwin, xcorrwin, stepsize	parameters as they were defined in section 4 of script B for the velocity computation.

Table E.2: List and explanation of all variables that are stored to the STAT-structure in order to allow easy analysis at any later point in time.

«Personal declaration: I hereby declare that the material contained in this thesis is my own original work. Any quotation or paraphrase in this thesis from the published or unpublished work of another individual or institution has been duly acknowledged. I have not submitted this thesis, or any part of it, previously to any institution for assessment purposes.»

Date & Place: .....

Signature: .....